

LA-UR-21-23050 (Accepted Manuscript)

Unraveling the Implications of Finite Specimen Size on the Interpretation of Dynamic Experiments for Polycrystalline Aluminum through Direct Numerical Simulations

Zuanetti, Bryan
Luscher, Darby Jon
Bolme, Cynthia Anne
Ramos, Kyle James

Provided by the author(s) and the Los Alamos National Laboratory (2021-08-09).

To be published in: International Journal of Plasticity

DOI to publisher's version: 10.1016/j.ijplas.2021.103080

Permalink to record: <http://permalink.lanl.gov/object/view?what=info:lanl-repo/lareport/LA-UR-21-23050>

Disclaimer:

Los Alamos National Laboratory, an affirmative action/equal opportunity employer, is operated by Triad National Security, LLC for the National Nuclear Security Administration of U.S. Department of Energy under contract 89233218CNA000001. By approving this article, the publisher recognizes that the U.S. Government retains nonexclusive, royalty-free license to publish or reproduce the published form of this contribution, or to allow others to do so, for U.S. Government purposes. Los Alamos National Laboratory requests that the publisher identify this article as work performed under the auspices of the U.S. Department of Energy. Los Alamos National Laboratory strongly supports academic freedom and a researcher's right to publish; as an institution, however, the Laboratory does not endorse the viewpoint of a publication or guarantee its technical correctness.

Journal Pre-proof

Unraveling the Implications of Finite Specimen Size on the Interpretation of Dynamic Experiments for Polycrystalline Aluminum through Direct Numerical Simulations

Bryan Zuanetti , Darby J. Luscher , Kyle Ramos , Cynthia Bolme

PII: S0749-6419(21)00152-2
DOI: <https://doi.org/10.1016/j.ijplas.2021.103080>
Reference: INTPLA 103080



To appear in: *International Journal of Plasticity*

Received date: 17 May 2021
Revised date: 5 August 2021

Please cite this article as: Bryan Zuanetti , Darby J. Luscher , Kyle Ramos , Cynthia Bolme , Unraveling the Implications of Finite Specimen Size on the Interpretation of Dynamic Experiments for Polycrystalline Aluminum through Direct Numerical Simulations, *International Journal of Plasticity* (2021), doi: <https://doi.org/10.1016/j.ijplas.2021.103080>

This is a PDF file of an article that has undergone enhancements after acceptance, such as the addition of a cover page and metadata, and formatting for readability, but it is not yet the definitive version of record. This version will undergo additional copyediting, typesetting and review before it is published in its final form, but we are providing this version to give early visibility of the article. Please note that, during the production process, errors may be discovered which could affect the content, and all legal disclaimers that apply to the journal pertain.

© 2021 Published by Elsevier Ltd.

Highlights

- Direct numerical simulations of dynamically compressed and/or sheared polycrystalline aluminum are carried out.
- The magnitude of the scatter in observable point measurements due to the heterogeneous microstructure is characterized.
- The grain size is shown to affect the inter and intra-granular distribution of state variables (e.g., velocity, plastic strain).
- The scatter decreases to zero (i.e., point measurements become representative of the mean-field) with decreasing grain size.
- The required number of grains per characteristic length for minimizing scatter is proposed.

Unraveling the Implications of Finite Specimen Size on the Interpretation of Dynamic Experiments for Polycrystalline Aluminum through Direct Numerical Simulations

Bryan Zuanetti^{1*}, Darby J. Luscher², Kyle Ramos¹, Cynthia Bolme¹

1) *Explosive Science and Shock Physics Division, Los Alamos National Laboratory, Los Alamos, NM, 87545, USA*

2) *Theoretical Division, Los Alamos National Laboratory, Los Alamos, NM, 87545, USA*

E-mail Addresses of Authors:

Bryan Zuanetti (bzuanetti@lanl.gov)

Darby J. Luscher (djl@lanl.gov)

Kyle Ramos (kramos@lanl.gov)

Cynthia Bolme (cbolme@lanl.gov)

**Corresponding Author*

ABSTRACT

Normal and Pressure-shear plate impact (NPI and PSPI) experiments are popular experimental techniques for studying the mean-field macroscopic behavior of polycrystalline metals under high-rate dynamic loading. However, since both configurations rely upon geometry for subjecting the specimen to high strain rates, these experiments often involve a limited specimen size. Moreover, because of the inherent heterogeneities present within polycrystalline metals, it is difficult to ascertain if the size of the specimen and/or regions where measurements are made are sufficiently large for making representative inferences about the mean-field macroscopic properties from single-point velocity measurements. In the present study, we quantify the expected measurement variability on observable point measurements in NPI and PSPI experiments by carrying out direct numerical simulations (DNS) of statistically representative

polycrystalline microstructures subjected to dynamic compression and compression-shear loading. In particular, we consider the role of specific material heterogeneities (e.g. the grain-to-grain difference in size, crystallographic orientation) on dispersion in the normal and transverse particle velocity records and on local fluctuations in key state variables (e.g. velocity, accumulated plastic strain) by incorporating these effects directly into a representative synthetic microstructure geometry and crystalline description of pure polycrystalline aluminum. The form of the present study is a large parametric investigation, consisting of ten ensembles of one hundred simulations. Each of the thousand simulations reflects a randomly realized synthetic microstructure in one of five cases of decreasing average grain size for the two loading configurations. Our analysis of the DNS results demonstrates that for both of these experimental configurations, the grain size directly correlates with the coefficient of variation (CV) in simulated point measurements, showing a convergent decrease in CV to zero (i.e. particle velocity record approaches the mean-field value) with decreasing grain size. Remarkably, the magnitude of variations in the particle velocity record is shown to be largest where the deviatoric stresses are most significant. In the case of NPI, this occurs at the elastic and plastic wavefront, whereas, in the case of PSPI, the magnitude of fluctuations are approximately constant throughout the experimental window time. The reasoning for the scatter in particle velocity due to the heterogeneous microstructure is demonstrated to be dependent on the mechanisms for accommodating deformation and on the interaction of reflection waves generated at sites of heterogeneities occurring at the scale of grains. Lastly, we develop a power-law description for the magnitude of scattering versus characteristic length, which provides a statistical framework for assessing the required number of grains per characteristic specimen dimension for minimizing scatter within these two experimental configurations (NPI, PSPI).

KEYWORDS

Shock compression; Pressure-shear; Plate Impact; dynamic experiments; plasticity; dislocations; single-crystal; polycrystal; isotropic; homogeneous; representative volume element; Direct numerical simulation; Solid mechanics; Aluminum

Journal Pre-proof

1. INTRODUCTION

Understanding the mechanics and physics of solids under extreme loading conditions is a fundamentally important challenge within material science for its relevance to a broad range of engineering applications that involve high deformation rates and transient temperatures. These applications routinely employ materials that are inherently heterogeneous at multiple scales. For example, engineered materials comprise several phases and/or aggregates of crystals with varying grain size and orientation. At smaller scales, features of the microstructure (e.g., alloying elements and defects) within the grain may be non-uniformly distributed. However, the length scales associated with engineered material systems are often large enough that macroscale models can be used to capture the salient features of the response (i.e., the mean-field macroscopic response), for instance, by using physics-based relations that represent the culmination of governing effects occurring at smaller scales [1-4]. Homogenization is a theoretical process by which macroscale models can be developed, which relies upon the notion of a representative volume element (RVE). The RVE can be described as the smallest volume of material such that further increases in material volume do not affect the observed intrinsic responses. The minimum size for the RVE (MSRVE) has been demonstrated to vary with material property [5] and although it has been studied for a wide range of materials [6-9], properties, and boundary conditions [10, 11], the MSRVE for dynamic properties (e.g., the Hugoniot elastic limit (HEL) and dynamic shearing/compressive resistance) is still incompletely addressed in the literature.

Experimental investigations aimed towards probing the mean-field macroscopic response of materials under high strain rates, pressures, and temperatures have also received significant

attention. Two experimental configurations amongst the many that are often employed for studying the mean-field macroscopic response of polycrystalline metals at high-to-very-high strain rates are normal (NPI) [12-14] and combined Pressure-shear (PSPI) Plate Impact [15-17]. In NPI, the dynamic strength and rate sensitivity of the response at incipient plasticity are inferred from the measurement of the arrival-time, amplitude, and profile of a relaxing elastic precursor wave (i.e., from normal free surface velocimetry). Whereas, in PSPI experiments, the effective dynamic shearing resistance is inferred from the transverse free surface velocimetry on an anvil plate. Since both configurations rely upon geometry to impose simple wave dynamics while subjecting the specimen to high strain rates, these experiments most often involve a limited specimen size. Moreover, because the sample behavior is typically inferred from point measurements using diagnostics with narrow spatial resolution and field-of-view (e.g., PDV [18], VISAR [19], NDI/TDI [20-22]) the size of the specimen and/or region where measurements are made may not be sufficiently large for its observed response to be representative of the mean-field macroscopic properties. In other words, it is unclear if the typical notion of an RVE is sampled in these dynamic loading experiments, because it is difficult to ascertain if the size of the specimen and/or regions where measurements are made are sufficiently large for making representative inferences about the mean-field macroscopic properties from single-point velocity measurements.

NPI experiments typically employ samples with a thickness on the order of millimeters. Other elastic precursor decay configurations, such as laser-driven shock compression, often employ samples with a sub-millimeter thickness [23-26]. On the other hand, PSPI experiments employ metallic foil samples of thickness on the order of few [27] to tens [15, 28, 29] of micrometers and a diameter on the order of tens of millimeters. In both configurations, velocimetry

measurements are typically obtained over a focused or collimated beam with a spot size on the order of tens to hundreds of micrometers. For measurements made at these scales, heterogeneities at scales smaller than the typical range of specimen size employed (e.g., from grain-to-grain differences in size, morphology, orientation) have been demonstrated to significantly affect the inferred macroscopic properties. For instance, NPI experiments have revealed that the dynamic yielding and spall properties of polycrystalline metals under planar shock loading are highly sensitive to grain size, morphology and orientation [30-33]. Modified VISAR techniques enabling particle velocity dispersion measurements to be made at the micro and mesoscale have revealed that the particle velocity profile is not uniform in experiments involving polycrystalline materials [34]. Planar shock studies on porous aluminum [34] high strength steel alloys [35] and aluminum alloys [36] conducted using this technique have revealed variance in the particle velocity profile of between 5 – 7% for measurements made over 70 – 100 micrometer spot size. Similar studies using line imaging and two-dimensional VISAR diagnostics have revealed non-uniform particle velocity distribution in other materials, such as plastically bonded explosives [37], and single crystal silicon [38], which highlight the persistent shortcoming of using a single point velocity measurement in the interpretation of the data from these experiments.

The reasoning for the non-uniformity of key variables (e.g. stress, velocity, temperature) in polycrystalline materials under normal shock compression have been studied theoretically and hypothesized to be due to the generation and interaction of multiple waves at sources of heterogeneities (e.g. from varying grain orientation, non-uniform distribution of defects or alloying elements) that may have a significant effect on the local substructure evolution and on the characteristics of the shock front [39-41]. And, although the magnitude of these effects have been estimated theoretically, these investigations most often incorporated Gaussian distributions

representing the average fluctuations of key variables of the model from hypothetical material effects [40, 42] rather than attempting to simulate these effects directly. More recent investigations have also employed single crystal plasticity models and looked at perturbations in the initial dislocation density as initiators for plastic strain localization [43].

For the PSPI configuration, experiments on foil specimens of polycrystalline metals made via vapor-deposition have been shown to exhibit enhanced shearing resistance when compared to thicker foil specimens made via traditional methods of the same material [27, 44]. Moreover, discrepancies have been observed when attempting to compare material properties inferred from PSPI to other experimental platform at similar rates. For example, micro Kolsky bar (μ KB) experiments conducted at similar rates to PSPI experiments, have exhibited enhanced sample-to-sample scatter in the data and smaller than expected shearing resistance than inferred in PSPI [45]. The explanation given for the discrepancy between the two experiments eluded to the possibility that μ KB samples may not have contained sufficient grains for being representative. However, PSPI foil specimens often contain a single or few grains through the thickness, but are often assumed to be representative due to their large lateral dimensions. The assumption that a PSPI experiment employing a limited specimen size with few grains through thickness can recover the representative response of a polycrystalline metal has not been validated in the literature until now. This question is of particular importance to the authors in the present study for its paramount significance to the interpretation of experimental data from PSPI.

Although these experiments have provided crucial insight into mechanisms governing the dynamic response of polycrystalline metals, the limited specimen size, spatial resolution, and field-of-view of the diagnostics employed render the contribution to the uncertainty of the

inferred macroscale properties ambiguous. These ambiguities in the inferred macroscale properties present clear challenges for both experimentalist attempting to measure a representative response of materials under extreme conditions and for modelers attempting to calibrate large parameter sets in more sophisticated models where scatter in the data could prevent the determination of unique parameter sets. Therefore, the present work aims to shed light on the expected measurement variability by explicitly investigating the role of heterogeneity (e.g., from the stochasticity of the microstructure and anisotropy of the crystal) on observable point measurements in NPI and PSPI experiments. In contrast to the theoretical studies discussed in the above, we study the role of specific material effects (e.g. grain-to-grain differences in crystal orientation creating both local elastic impedance mismatches, and local variations in plasticity associated with preferential orientations for accommodating slip) by incorporating these directly into the synthetic microstructure geometry and in the crystalline material description. The DNS results provide a statistical basis for assessing measurement variability within these two experimental configurations (NPI, PSPI). For this, we make use of a crystalline thermoelastic-viscoplastic description of pure annealed aluminum to perform direct numerical simulations (DNS) of statistically representative microstructures within macroscale polycrystalline specimens subjected to dynamic compression and compression-shear loading.

A few of the pertinent questions which we address in the present study are:

- Does microstructure grain size cause appreciable variability of point measurements in NPI and PSPI experiments?

- Do point velocity measurements from NPI and PSPI show a convergent behavior towards a single mean-field value as the grain size is reduced for typical ranges of specimen size and microstructure?
- Can we quantify the uncertainty of the inferred macroscale properties resulting from heterogeneities at smaller scales?

The current manuscript is structured as follows. In Sec. 2, we provide details about the modeling approach, including a review of the continuum description of the material, generation of representative microstructure, and plane wave simulation schemes. The results from DNS are presented and discussed in Sec 3, showing the effect of grain size on the variability of point measurements in NPI and PSPI simulation schemes. Finally, we summarize the main points of our findings in Sec. 4.

2. MODELING METHODS

The low number of impurities and defects present within pure annealed metals are expected to limit the contributions from sub-grain scale heterogeneity relative to intergranular fluctuations on observed variability at the macroscale. For this reason, we employ a continuum single crystal thermoelastic-viscoplastic model for describing the response of the individual pure aluminum grains. We further stipulate a uniform distribution of dislocations within each grain, which we believe to be a reasonable constitutive approximation for the case of pure annealed metals. Hence, the initial source of heterogeneity within these simulations are the grain-to-grain differences in crystal orientation which creates both i) local elastic impedance mismatches, and ii) local variations in plasticity associated with preferential orientations for accommodating slip.

2.1 Review of the continuum description of the material

We employ an extension of a previous isotropic viscoplastic model [3, 29] adapted to represent the anisotropic thermomechanical response of individual crystals during shock compression within simulations using our fully Lagrangian finite element code. It is derived from previous models of Austin and McDowell [3, 46] and Lloyd et al [47] for polycrystalline and single-crystal aluminum, respectively. It is intended that the single-crystal model used here is consistent with the previous isotropic viscoplastic model of Zuanetti et al. [29] in the isotropic limit. Thus, our model assumptions made here are not necessarily intended to achieve a close calibration to any specific set of single crystal aluminum measurements.

Details of the relevant single crystal theory can be found in detail elsewhere [1, 47-49] and are only briefly summarized in this section and in **Appendix A**. A finite-element based hydrocode

provides the total deformation gradient, $\mathbf{F} = \frac{\partial \mathbf{x}}{\partial \mathbf{X}}$, consistent with $\mathbf{L} = \dot{\mathbf{F}}\mathbf{F}^{-1}$. The total deformation gradient is decomposed into separate parts representing the elastic lattice deformation, \mathbf{F}_e , and the cumulative effects of dislocation-accommodated crystalline slip, \mathbf{F}_p , according to $\mathbf{F} = \mathbf{F}_e\mathbf{F}_p$. The plastic part of the deformation gradient is evolved via the conventional crystal plasticity expression

$$\bar{\mathbf{L}}_p = \sum_{\alpha=1}^{N_s} \dot{\gamma}^\alpha (\mathbf{s}_o^\alpha \otimes \mathbf{n}_o^\alpha) \#(1)$$

defined in the intermediate configuration. \mathbf{s}_o^α and \mathbf{n}_o^α are the vectors normal to the slip plane and along the slip direction for the α -th slip system, respectively, and the slip rate on the slip system is defined by the Orowan expression, i.e., $\dot{\gamma}^\alpha = g_m^\alpha b^\alpha v^\alpha$. Here, b is the magnitude of the Burgers' vector and g_m^α and v^α are the density of mobile dislocations and their mean velocity, respectively, for the α -th slip system. Expressions for the evolution of mobile dislocations and their corresponding velocity are those developed by Lloyd et al. [47], with the exception of the dislocation multiplication rate, which here is adapted from the relationship of Gilman [50] in order to maintain consistency with the previous model of Zuanetti et al. [29] in the isotropic limit. The rate of change of the density of mobile dislocations is given by

$$\dot{g}_m^\alpha = \dot{g}_{\text{het}}^\alpha + \dot{g}_{\text{mul}}^\alpha - \dot{g}_{\text{ann}}^\alpha - \dot{g}_{\text{trap}}^\alpha \#(2)$$

The density of mobile dislocations is taken to increase due to the nucleation of dislocations at heterogeneous sources $\dot{g}_{\text{het}}^\alpha$, and dislocation multiplication, $\dot{g}_{\text{mul}}^\alpha$, associated with interactions of dislocations with forest dislocations (i.e., acting as Frank-Read sources). The rate of mobile

dislocations is reduced by the rate of dislocation annihilation, $\dot{\rho}_{\text{ann}}$, contained in the same plane and of opposite polarity and also by immobilization, $\dot{\rho}_{\text{trap}}$, due to being trapped through interactions with forest dislocations. The rate of heterogeneous nucleation is given by

$$\dot{\rho}_{\text{het}} = \alpha_{\text{het}} f(\tau^\alpha) \langle \dot{\tau}^\alpha \text{sign}(\tau^\alpha) \rangle \#(3)$$

where

$$f(\tau^\alpha) = \begin{cases} \frac{m+1}{(\tau_a - \tau_b)} \left(\frac{|\tau^\alpha| - \tau_a}{\tau_a - \tau_b} \right)^m & \tau^\alpha \in [\tau_a, \tau_b] \\ 0 & \text{otherwise} \end{cases} \#(4)$$

The Macaulay brackets in the Eq. (3) are implemented to ensure that heterogeneous nucleation only takes place if the rate of stress acts to increase the magnitude of the resolved shear stress.

The remaining terms for mobile dislocation evolution are taken to be as follows: $\dot{\rho}_{\text{mul}}^\alpha = C_M g_m^\alpha |v^\alpha|$, $\dot{\rho}_{\text{ann}}^\alpha = C_A (g_m^\alpha)^2 |v^\alpha|$, $\dot{\rho}_{\text{trap}}^\alpha = C_T \sqrt{g_f^\alpha} g_m^\alpha |v^\alpha|$, where τ_a , τ_b , m , α_{het} , C_M , C_A , and C_T are material specific model parameters.

The expression for the evolution of immobile dislocations is

$$\dot{\rho}_{\text{im}}^\alpha = F_{\text{im}}^\alpha \dot{\rho}_{\text{trap}}^\alpha \#(5)$$

The immobile dislocation density grows proportionally to the rate of trapping by a scalar function F_{im}^α , which has been adapted in order to maintain consistency with the previous model of Zuanetti et al. in the isotropic limit, and represents the effects of temperature/rate-dependent dynamic recovery [29]. Here, the dynamic recovery function is taken to be

$$F_{im}^{\alpha} = \left[1 - \left(\frac{\varrho_{im}^{\alpha}}{\varrho_{s_{im}}^*} \right)^{m_{rec}} \right] \#(6)$$

where

$$\varrho_{s_{im}} = \varrho_{s_0} \left(\frac{\varrho_m^{\alpha} b^{\alpha} v^{\alpha}}{\dot{\gamma}_0} \right)^{\frac{\alpha_{rec} T}{T_0}} \#(7)$$

Where, m_{rec} , ϱ_{s_0} , $\dot{\gamma}_0$, and a_{rec} are model parameters, and ϱ_{si}^* is the effective immobile dislocation saturation limit, and is defined as

$$\varrho_{s_{im}}^* = \left(\varrho_{s_{im}}^2 + \varrho_a^2 \right)^{\frac{1}{2}} \#(8)$$

The form of Eq. (8) ensures that the immobile dislocation density never decreases below, ϱ_a , the estimated dislocation density for a fully annealed sample.

2.2.1 Model Parameters

The physical/thermal and single crystal elastic constants for aluminum for the thermoelastic free energy are provided in **Table 1**. Isentropic second-order elastic constants are obtained from hydrostatic compression data on single crystal aluminum from the literature [47, 51, 52]. The differences between isentropic and isothermal elastic constants are negligible to the purposes of this investigation. The density, specific heat capacity, and volumetric thermal expansion coefficient were obtained from an experimental study performed by Raju [53]. We employ a Mie-Gruneisen equation of state (EOS) [54] to define the volume-pressure aspect of the Helmholtz free energy. The parameters for the EOS were identified by fitting shock

compression data on commercial purity aluminum provided in the LASL shock Hugoniot handbook [55] and from Austin [56] for pure polycrystalline aluminum.

Table 1. Relevant physical/thermal properties and modeling parameters for the elastic and purely volumetric response of polycrystalline aluminum.

Parameter	Value	Units	Description
C_{11}	106.8×10^9	Pa	Second order elastic constant
C_{12}	60.4×10^9	Pa	Second order elastic constant
C_{44}	28.3×10^9	Pa	Second order elastic constant
ρ_o	2700	Kg/m ³	Initial Density
k	205	W/m·K	Isotropic thermal conductivity
c_o	900	J/kg·K	Initial specific heat capacity
α_{v_o}	69.9×10^{-6}	1/K	Volumetric thermal expansion coefficient
C_o	5386.0	m/s	Bulk wavespeed
a	1.49	---	Mie-Grüneisen EOS parameter, a
s_1	1.339	---	Mie-Grüneisen EOS parameter, s_1
s_2	0.0	---	Mie-Grüneisen EOS parameter, s_2
s_3	0.0	---	Mie-Grüneisen EOS parameter, s_3
γ_o	1.97	---	Grüneisen gamma

The relevant parameters pertaining to the single crystal plasticity model are provided in **Table 2**. Values for most of these parameters were selected to be consistent with our previous modeling of polycrystalline aluminum [29], or obtained directly from literature on single crystal aluminum [46, 47, 56, 57]. For example, the parameters for the Kocks free enthalpy of activation (e.g., the effective shear modulus, thermal depinning parameters, dislocation energy barrier coefficient, athermal threshold stress), effective drag coefficient (Phonon drag fitting and normalization parameters), as well as the parameters contributing the heterogenous nucleation and recovery rates, are taken from our previous work on polycrystalline aluminum [29]. The remainder of the parameters, which contribute to the threshold stress for dislocations to overcome short-ranged barriers (barrier spacing, dislocation-dislocation interaction), and the evolution of mobile and

immobile dislocation populations (multiplication, immobilization, annihilation) are identified via a manual calibration procedure so that the mean response from an ensemble of DNS simulations reasonably agrees with NPI and PSPI experimental records on polycrystalline aluminum [29, 58]. These parameters, (i.e., the barrier spacing scaling parameter, dislocation-dislocation interaction coefficient, dislocation multiplication, annihilation, immobilization coefficients) closely accord with values in the literature for single crystal aluminum. [46, 47, 59].

Journal Pre-proof

Table 2. Single crystal plasticity model parameters for pure aluminum.

Parameter	Value	Units	Description
τ_{ath}	0.01×10^9	Pa	Athermal threshold stress
b	2.86×10^{-10}	m	Burger's vector
ν_d	1.00×10^{13}	s^{-1}	Debye frequency
g_o	0.5	---	Energy barrier parameter
\bar{p}	0.4	---	Thermal depinning parameter
\bar{q}	2.5	---	Thermal depinning parameter
$\bar{\alpha}$	0.064	---	Barrier spacing scaling parameter
h	0.6	---	Dislocation-dislocation interaction coefficient
θ	230	K	Phonon drag normalization factor
B_o	1.051×10^{-5}	Pa·s	Phonon drag normalization factor
a_0	0.0	---	Phonon drag fitting parameter
a_1	1.0	---	Phonon drag fitting parameter
a_2	0.0	---	Phonon drag fitting parameter
a_3	0.0	---	Phonon drag fitting parameter
a_4	9.50×10^{-3}	---	Phonon drag fitting parameter
μ_{eff}	27.1×10^9	Pa	Steinberg-Guinan Shear Modulus $P = 0, T = T_{ref}$
μ_p/μ_o	6.52×10^{-11}	Pa^{-1}	Pressure dependence parameter
μ_T/μ_o	-6.16×10^{-4}	K^{-1}	Temperature dependence parameter
α_{het}	1.2886×10^{14}	m^{-2}	Dislocation heterogeneous nucleation coefficient
m_o	0.85	---	Heterogeneous nucleation PDF parameter
τ_a	20.0×10^6	Pa	Threshold for heterogeneous nucleation (lower)
τ_b	1.80668×10^9	Pa	Threshold for heterogeneous nucleation (upper)
C_M	4.50×10^5	m^{-1}	Dislocation multiplication coefficient
C_A	0.5	---	Dislocation annihilation coefficient
C_T	2.1×10^{-2}	---	Dislocation immobilization coefficient
$\rho_{initial}$	1.00×10^{11}	m^{-2}	Initial dislocation density
f_m	0.50	---	Ratio of dislocation densities (mobile/immobile)
ρ_{isat_0}	1.2×10^{15}	m^{-2}	Immobile saturation limit coefficient
$\bar{\gamma}_0$	5.0×10^6	s^{-1}	Recovery function normalization factor
α_{rec}	0.9	---	Recovery function scaling parameter
m_{rec}	1.0	---	Recovery function scaling parameter

2.2 Generation of polycrystalline microstructure geometry

In order to realize the polycrystalline microstructures with uniformly random grain orientations and equiaxed grains of a desired size, we employ the open source python package MicrostructPy [60, 61] for statistical microstructure mesh generation. An example of a random polycrystalline geometry and the corresponding inverse pole figure is shown in **Figure 1**. The microstructure geometry depicted in Fig 1 was generated using a modified Laguerre-Voronoi tessellation within MicrostructPy. Seeds were randomly placed in a rectangular domain such that circles, whose diameter corresponds to the average grain size, associated with each seed are not allowed to overlap beyond a specified tolerance. The overlap tolerance is chosen automatically by the MicrostructPy for improving the correlation between the seed and grain volumes.

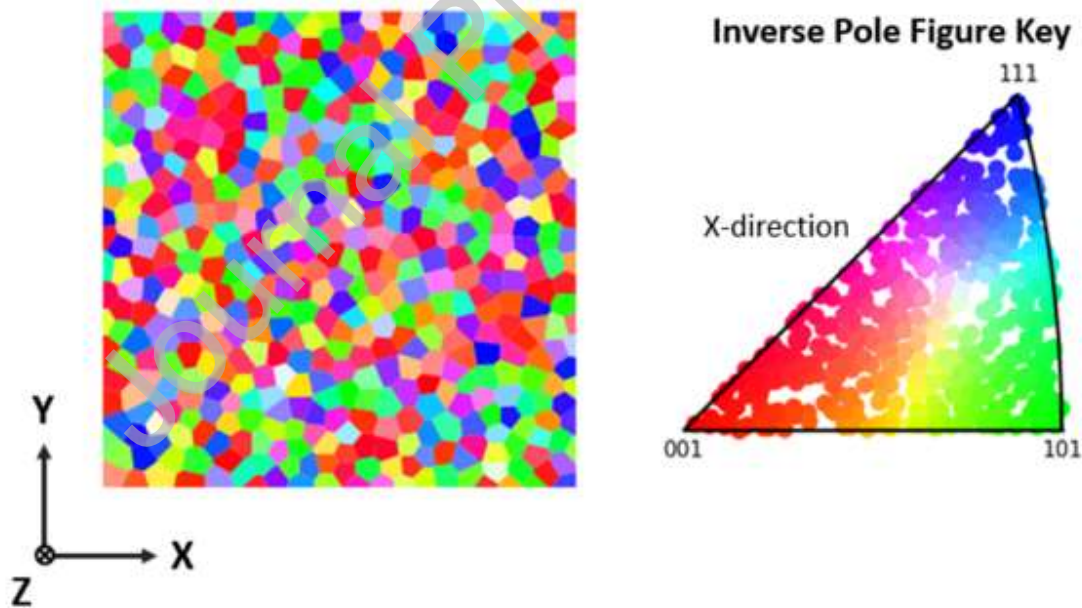


Fig 1. An example of random polycrystalline microstructure geometry showing uniformly distributed equiaxed grains with no preferential orientation (left), and the corresponding inverse pole figure (IPF) (right). The color in the IPF represents the alignment of the crystal axis with the x-direction, which is chosen to be the wave propagation direction in all simulations presented in this manuscript.

Each Voronoi cell corresponds to a single crystal whose orientation is randomly drawn from a uniform distribution over $SO(3)$ [62] yielding no preferential orientation within the domain. The resulting grains are relatively equiaxed, have no preferential orientation, and possess a size that is proximate to the user-specified seed diameter size.

Continuum models of microstructure often use a conforming unstructured mesh in two- or three-dimensions in order to align element boundaries with grain boundaries without much geometric approximation [63-65]. However, this approach can lead to complications including degenerate or poorly shaped elements in numerical simulations involving large deformations, such as in the case of PSPI. Simulations of impact response in microstructure using such meshes often suffer from numerical impedance mismatches and mesh imprinting [65]. To circumvent these potential issues, we employ a pixel approximation of the original microstructure geometry by a structured hexahedral mesh, as shown in **Figure 2**. This approach has been shown to provide adequate accuracy in reproducing stress distributions at the scales of interest with improved efficiency and simplicity over a smooth topological representation [66]. This approach has also been successfully employed in a similar DNS study performed by Bishop et al. [67] for investigating the macroscale effects of microstructural variability in structural applications.

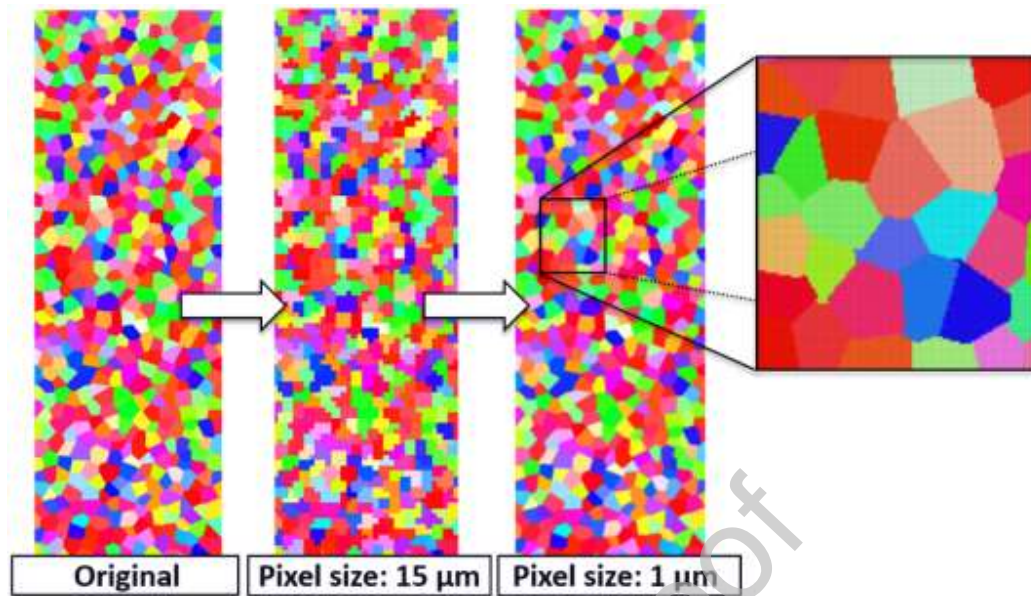


Fig 2. Pixelization of a synthetic microstructure geometry in NPI simulations. The final pixel size of $1\ \mu\text{m}$ was chosen after successive refinements until properties of interest (i.e., features of the normal free surface particle velocity record) converged within 2 percent for representative simulations.

As shown in **Fig 2** the final pixel approximation of the microstructure geometry was chosen after successive refinements until the rastered image adequately recovered the geometry of the grains and properties of interest (i.e., features of the normal free surface particle velocity record) converged within 2 percent for representative simulations.

2.3 Plane wave simulation schemes

The DNS of polycrystalline samples using the single-crystal material model (described in **Section II a**) are implemented within a total Lagrangian finite element code. A detailed description of the FEM code used in this work is provided in [29]. Briefly summarize here, the code employs fully three-dimensional reduced-integration eight-noded elements comprising of isoparametric shape functions for solving the global-level discrete algebraic equations of motion

and temperature evolution. The equation of motion is integrated in time using an explicit beta-Newmark method [68] and the coupling between thermal and mechanical fields is performed via a staggered solution procedure [69]. To limit the errors accumulated due to large changes in deformation over a time step, a fully explicit fourth order Runge-Kutta scheme is employed for updating the plastic part of the deformation gradient and internal evolving state variables of the model in the hyperelastic stress update algorithm.

For all simulations discussed here, the entire simulation domain is comprised of a three-dimensional hexahedron and is filled using a structured mesh of eight-node hexahedral elements (bricks), as illustrated in **Figure 3**.

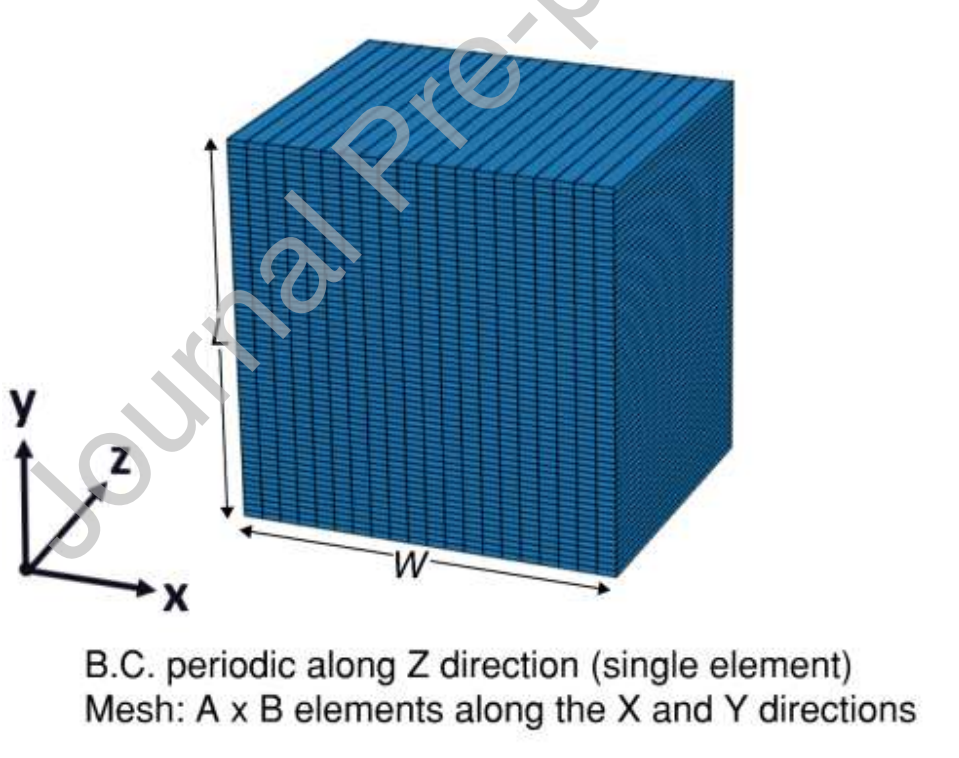


Fig 3. The structured mesh is comprised of a hexahedron volume filled with $A \times B \times 1$ 8-noded hexahedral elements (bricks) along the X, Y, Z directions, respectively. For all the simulations presented in this manuscript, a single element comprises the depth in the Z direction and periodic boundary conditions are applied in this direction to avoid boundary wave effects from the free surfaces along z-axis. The length, L and width, W are determined by the sample/anvil geometry.

The 2D geometry was discretized into a single layer of 3D elements with periodic boundary conditions applied on the extremal surfaces of z-axis. Subsequent illustrations of the simulation schemes/mesh are shown with a viewing direction coincident with the Z-direction.

The model geometries for simulating normal and combined pressure-and-shear plate impact experiments are shown in **Figure 4**. The sample dimensions and boundary conditions for the NPI simulations (shown in **Fig 4a**) were selected to be consistent with work of Zuanetti et al. [29] to enable comparison with that previous work. Accordingly, the sample constitutes the entire grid, the normal particle velocity of 200 m/s is prescribed at the surface $X = 0$ for the duration of the simulation, while the remainder of the body is prescribed to be initially at rest and at a temperature of 296 K. The specimen possesses a length, L , and width, W , of 0.5 mm and 1.5 mm, respectively. Note that the Width of 1.5 mm is chosen such that boundary waves do not appear at the measurement point (taken to be at the center of the free surface at $X = L$, and $Y = 0.5D$) through the duration of the simulation, 0.125 μ s. In the PSPI simulations (shown in **Fig 4b**), for comparison purposes, the sample dimensions and boundary conditions are selected consistent with the PSPI01 experiment presented previously [29]. The simulation domain comprises a thin rectangular region representing the polycrystalline aluminum sample and a thick WC anvil plate. The elastic behavior of the anvil plate is represented as linearly elastic and possess a density, first Lamé parameter, and shear modulus of 15,400 kg/m³, 150 GPa, and 287 GPa, respectively [70]. The normal and transverse particle velocity of 97.35 and 39.33 m/s are prescribed at the surface $X = 0$ for the duration of the simulation, while the remainder of the grid is prescribed to be initially at rest and at a temperature of 296 K. The sample and anvil dimensions are 0.07 mm and 6.0 mm in length, respectively, and have a width of 40 mm such

that boundary waves do not appear at the measurement point through the duration of the simulation, 2.3 μs .

The optimal number of elements and time step size for computational efficacy were determined via a mesh convergence analysis involving successive mesh refinements until properties of interest (i.e., features of the normal and transverse free surface particle velocity record) converged within 2 percent for representative simulations. Accordingly, the X and Y element dimensions of 1 μm and a time step of 30 picoseconds were selected for NPI simulation schemes. For the PSPI simulation scheme, due to the much larger Y dimension of the grid and lower strain-rates involved. The Y dimension of the element was selected to be 40 μm while the X dimension was maintained at 1 μm for the sample. Also, a pixel size of approximately 10 μm was chosen for the anvil plate. This size was chosen after successive refinements to prevent artificial impedance mismatch, wave dispersion, and/or the introduction of numerical waves. A timestep size of 90 picoseconds was used for the PSPI simulation.

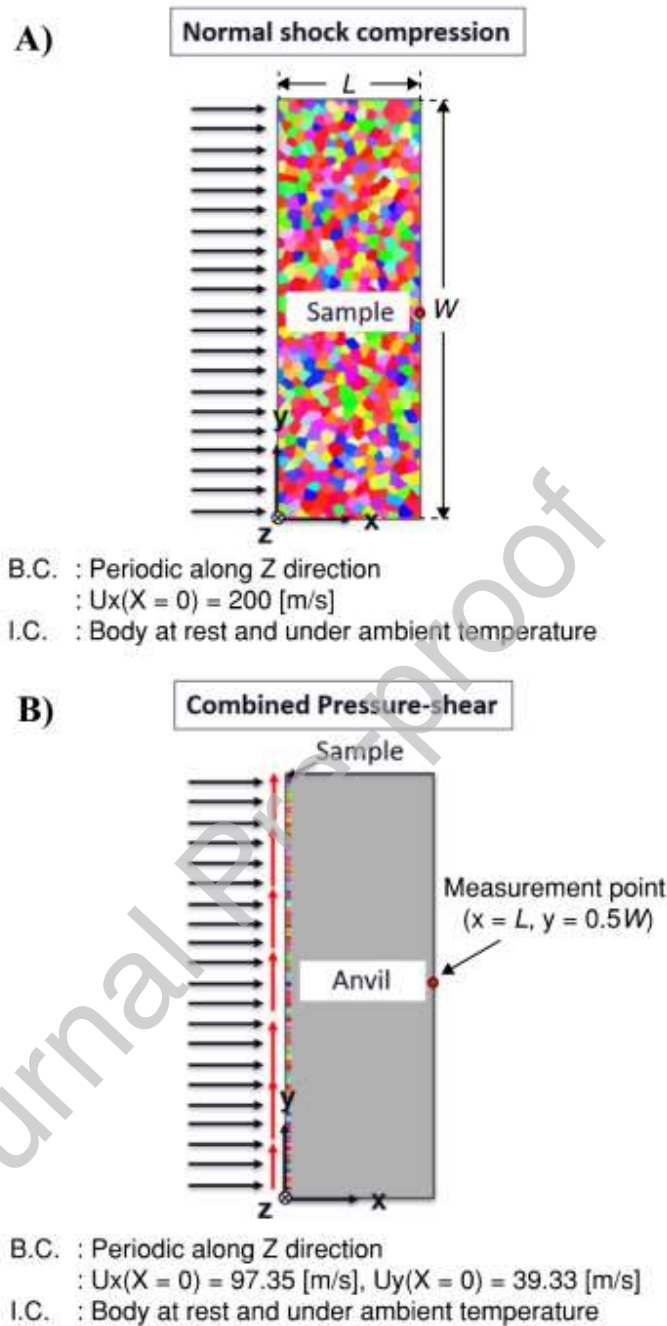


Fig 4. Planar wave simulation schemes for **a)** Normal shock compression, and **b)** combined pressure-shear simulations. In **a)** the sample is represented by the entire grid, whereas for **b)** the sample is a thin rectangular region on the front surface of a fully elastic anvil plate). In both configurations, the bodies are initially at rest and at a temperature of 296 K, and the particle velocities at $x = 0$ are specified as boundary conditions. Free surface particle velocity records reported herein are obtained at the center of the free surface denoted by the red circle (i.e., at $x = L$, and $y = 0.5W$, where L and W are the length, and width of the grid respectively). In NPI simulations, the entire grid is comprised of the sample, hence, $L = 0.5$ mm and $W = 1.5$ mm. In

PSPI simulations, the grid is comprised of the sample and anvil, hence, $L = 6.07$ mm and $W = 40$ mm.

Journal Pre-proof

3. RESULTS AND DISCUSSION

In the current study, two series of simulations were carried out and are reported (i.e., one series for NPI and for PSPI, respectively). For each series, there are several simulation cases (A-D for NPI and A-E for PSPI) containing an ensemble of one-hundred realizations per case. Each case has a different average grain size, refined successively with increasing alphabetical order. Each simulation employs a different random microstructure geometry and associated random uniform distribution of grain orientations. Moreover, the sample/target configuration and dimensions for all cases are consistent with their respective description provided in **Section 2.3**. These dimensions were chosen primarily for comparative purposes with the NPI and PSPI experiments presented in our previous work [29]. In the following sections we discuss the results of these simulations in the context of the effects of microstructure on the variability of observable measurements in NPI and PSPI experiments.

3.1 Normal shock compression of synthetic polycrystalline aluminum

In NPI experiments, at impact, an infinitesimally small volume of material at the load interface is subjected to extremely high strain-rate compressive uniaxial strain loading. During the loading process, this infinitesimal volume of material initially deforms elastically, however, due to the extremely high deviatoric stresses the material subsequently flows. Plastic flow relaxes the deviatoric stresses which evolves the state of stress towards a nearly hydrostatic state (i.e., a state in which the deviatoric stresses become insufficient to cause continued plastic flow). If the wave speed associated with the characteristic line joining the initial and final Hugoniot (pressure, particle velocity) states under the particular impact conditions is lower than the longitudinal

wave speed at incipient plastic flow, then the process will result in propagation of two waves including an elastic precursor wave traveling at the longitudinal wave speed, followed by a subsequent shock wave traveling at a lower speed determined by the jump from HEL to final Hugoniot states. As the elastic precursor wave continues to propagate through the sample, its amplitude is proportional to the deviatoric stress component and continues to decrease due to the ongoing plastic flow behind the precursor front. The rate of attenuation is proportional to the amplitude of the resolved shear stress; hence, the elastic precursor decreases at an exponentially decaying rate. After a sufficiently large propagation time/distance the precursor amplitude becomes nearly steady.

Previous work has focused on the rate of relaxation of the elastic precursor amplitude over a wide range of propagation lengths as a characteristic response of a material [23-25, 29, 71]. For NPI experiments involving polycrystalline specimens, this observed rate of relaxation has contributions from multiple uniquely deforming grains which are sampled at different lengths/times as the wave propagates across the sample. The simulations presented below are designed to reveal i) the effect of grain size on the dispersion in the normal particle velocity history, ii) if the rate of relaxation after a relatively short length/time (i.e., prior to reaching a quasi-steady wave profile) becomes representative of a mean-field value as the grain size is reduced.

For NPI simulations, the representative microstructure geometries for cases A through D are provided in **Figure 5** along with its corresponding inverse pole figure. The color and position of a point on the IPF indicates the alignment of the global X-direction, which is coincident with the predominant wave propagation direction, with respect to crystallographic lattice plane normal.

These inverse pole figures confirm that there is no preferred orientation for grains. The average, \bar{G} , and standard deviation, σ , of grain size for cases A, B, C, D are $191.8 \pm 52.9 \mu\text{m}$, $94.3 \pm 32.4 \mu\text{m}$, $47.3 \pm 17.1 \mu\text{m}$, $32.9 \pm 12.5 \mu\text{m}$, respectively.

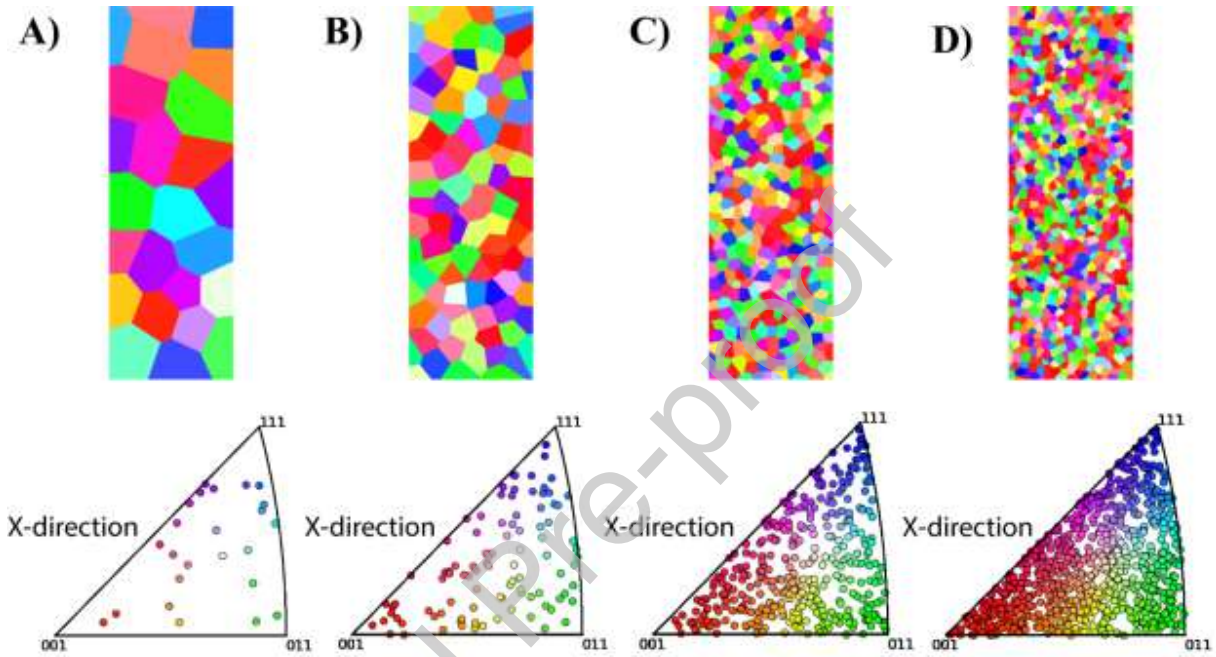


Fig 5. A representative microstructure geometry and corresponding inverse pole figure for the four simulation cases of NPI experiments. The average grain size for case A, B, C, D are $191.8 \mu\text{m}$, $94.3 \mu\text{m}$, $50 \mu\text{m}$, $35 \mu\text{m}$, respectively. The color and position of the point on the IPF indicate the alignment of the respective crystallographic direction of the grain with the global X-direction. There is no preferred orientation for these simulations.

3.1.1 The effect of grain size on dispersion in the normal particle velocity history

The particle velocity records at the center of the free surface, depicted as a red circle in **Fig 4a**, for all cases are presented in **Figure 6**. Here, light gray curves represent individual realizations, and the solid black curve is the ensemble average. The inset provides a clear view of the region surrounding the HEL. In every simulation, the normal free surface particle velocity record

reveals a two-wave structure, comprising of the arrival of the elastic precursor wave followed by the trailing shock wave. Later, the profile becomes nearly steady reaching the shock plateau. The figure shows noticeable variations in the particle velocity record in each of these regions. In particular, there are variations in the arrival time, upper and lower values of the HEL, post-HEL particle velocity rise, and in the shock plateau. The magnitude of these variations decreases with decreasing grain size.

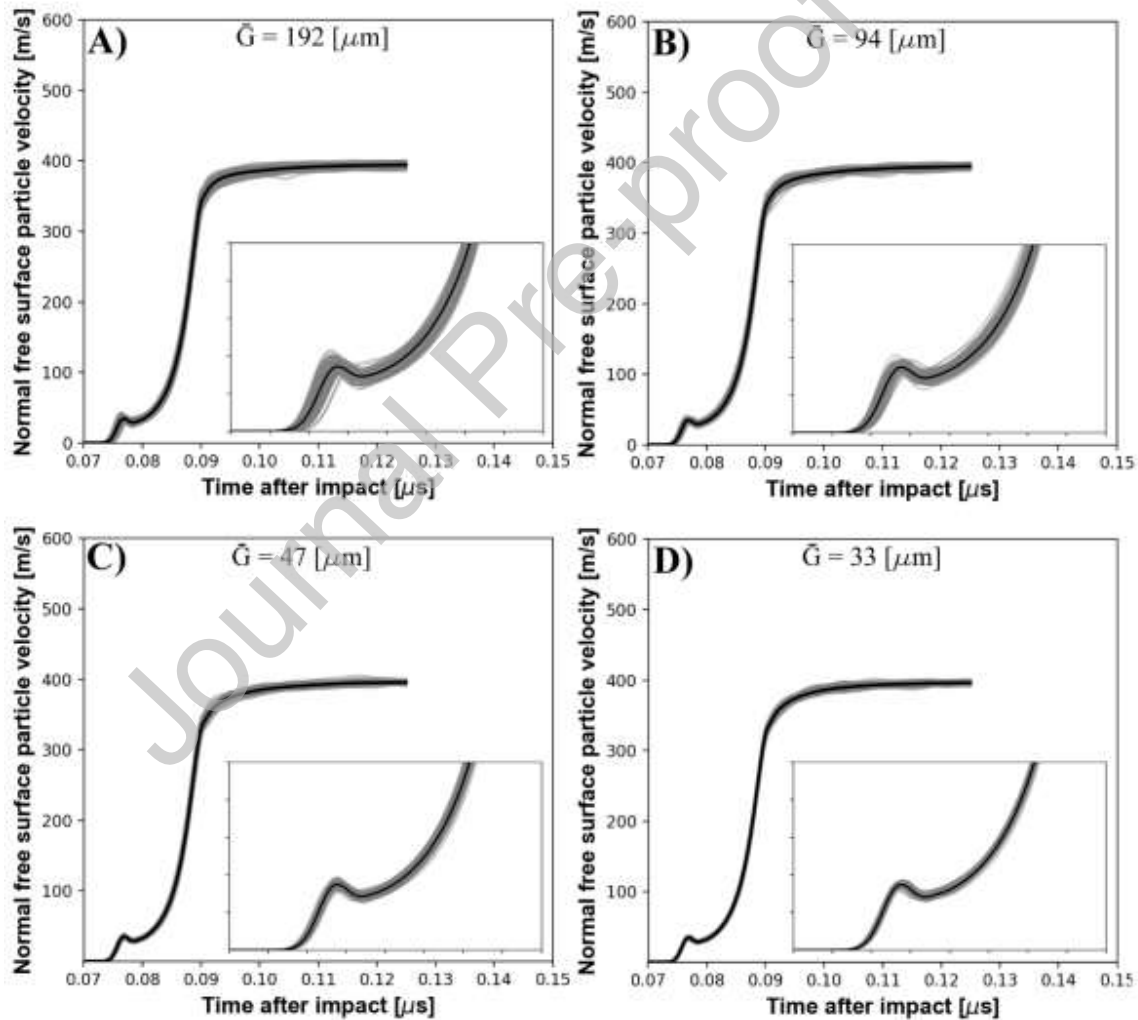


Fig 6. Particle velocity history at the center of the free surface of the sample (i.e., $X = L$, $Y = 0.5D$) for each case **A-D** in the normal shock compression series. The semi-transparent colored curves represent individual realizations for each case and the solid black curve is the average of

the ensemble of simulations for the respective case. The inlay shows a zoomed in region around the HEL.

We plot the mean and coefficient of variation (CV) (taken as the ratio between the standard deviation and the mean) at all times for each ensemble in **Figure 7** to quantify the evolution and significance of this scatter in the free surface particle velocity history.

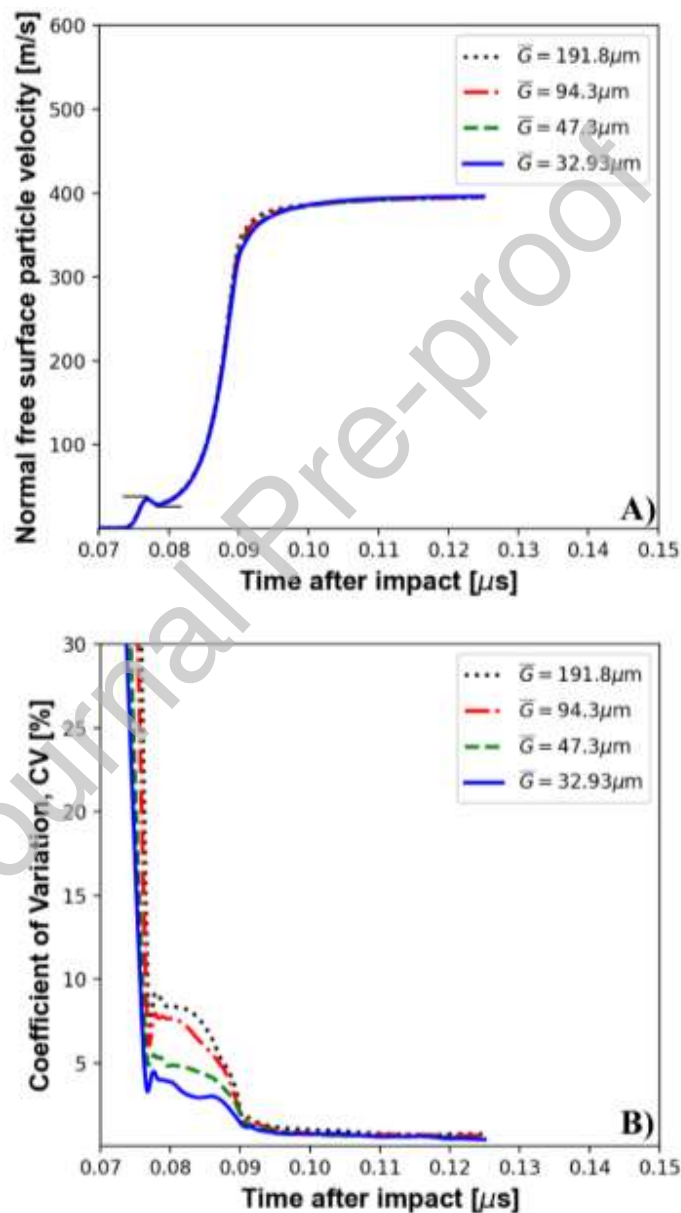


Fig 7. The mean **A**) and coefficient of variation **B**) (i.e., the ratio between the standard deviation and the mean) for the ensemble of simulations of each respective case versus time after impact.

A) shows that the mean for all cases is nearly identical, with its largest difference (of less than 1%) being just prior to the shock plateau. **B)** Shows that the CV decreases successively with decreasing grain size, \bar{G} .

Fig 7a shows that the ensemble average response for each case is nearly coincident, showing its largest discernable difference (less than 2%) in the narrow region prior to the shock plateau. **Fig 7b** shows that the CV successively decreases with decreasing average grain size. Two particularly striking features of **Fig 7b** are that i) the CV after the arrival of the elastic precursor wave is largest across the shock front, and ii) the CV continues to decrease with time reaching its smallest value (below 1%) at the end of the experimental window. A physical explanation for these observations is that the CV depicting the scatter due to heterogeneous microstructure is largest where the deviatoric stresses are most significant. This suggests that the CV is less significant at the shock plateau because i) most deviatoric stress has been relaxed and the Hugoniot state is largely dependent on the hydrostatic equation of state, and ii) the particle velocity is large relative to the fluctuations due to the heterogeneous microstructure.

To demonstrate this effect, we plot the history of the standard deviation, σ , in **Fig 8a** and compare this to the history of the equivalent deviatoric stress, $\bar{\sigma}$, in **Fig 8b** obtained from a comparable simulation using the isotropic model of Zuanetti et al. [29]. It can be observed in **Figure 8**, that the two histories are concurrent. This result can be easily explained within the context of the present material model, since the anisotropy in the crystalline material description is captured in Helmholtz free energy through the coupled volumetric/deviatoric term and energy stored within the lattice associate with slip (i.e. the two rightmost terms in A.13). Hence, the conditions i) and ii) can also be expressed in terms of the Helmholtz free energy in the model, as the condition when the purely volumetric contribution (i.e., coming solely from EOS, A.14) to the total free energy is much larger than the remaining terms. This result is significant because it

implies that the scatter associated with the heterogeneous microstructure would become less significant with increasing hydrostatic pressure for shocked aluminum.

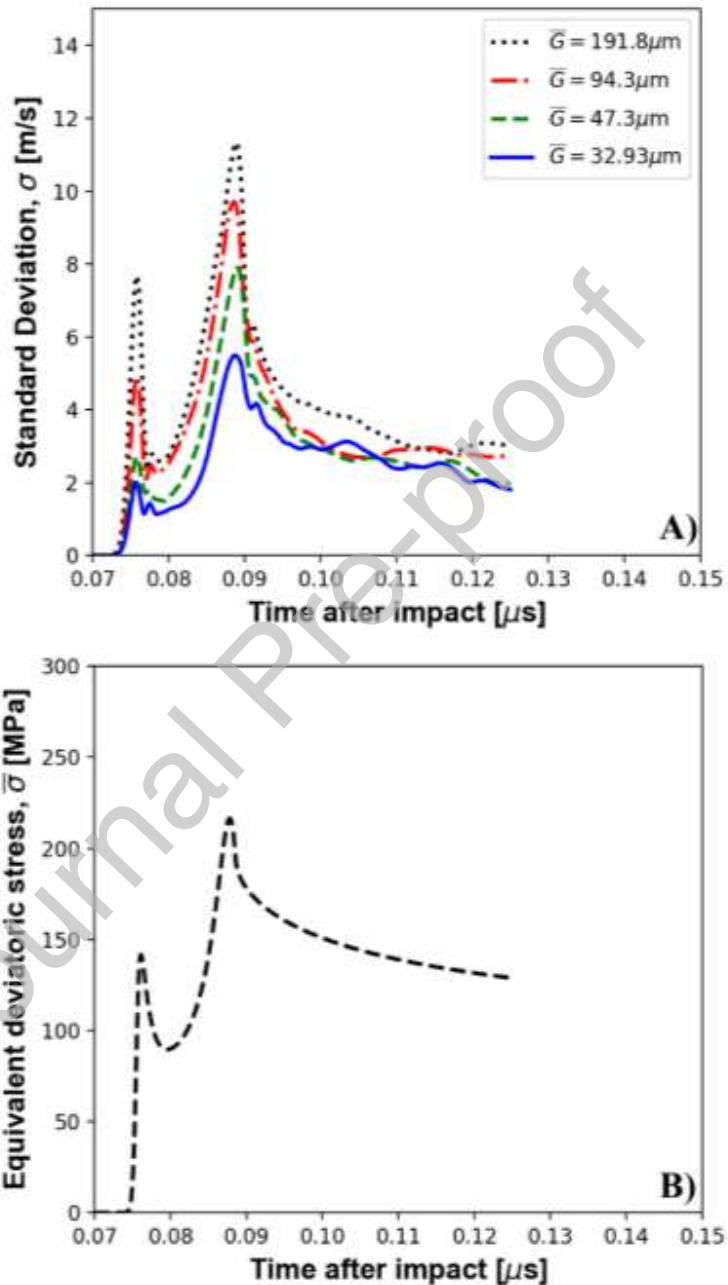


Fig 8. The standard deviation A) in the free surface particle velocity history for ensembles of each respective case of decreasing grain size. And, B) the history of the equivalent deviatoric stress obtained from a comparable simulation using the isotropic model of Zuanetti et al. [29].

The plot reveals that the standard deviation depicting the scatter due to the heterogeneous microstructure is largest where the deviatoric stresses are largest.

It is noteworthy to mention that the standard deviation history obtained in the present simulations are remarkably similar in magnitude and shape in comparison to the particle velocity dispersion curves (i.e. proportional to the standard deviation) of a shocked D-16 aluminum alloy measured experimentally by Divakov et al. [36], giving credence to the simulation results. The reasoning for the shape of these curves can be readily explained by considering the time evolution of key variables in the plasticity model contributing to the strength of the material. This has been discussed in detail in our previous work [29] so we only succinctly review them here. In a typical NPI experiment, at the arrival of the longitudinal wave, the mechanical threshold stress (i.e., the stress required for dislocations to overcome an opposing obstacle strength associated with short-range obstacles and athermal stress) is lower than the deviatoric stress provided by the loading conditions. Under these conditions, dislocations are provided enough energy to easily overcome short-range obstacles, hence, the major contribution to the flow stress comes from the opposition to dislocation glide due to the phonon viscosity. The initially high drag stress opposing dislocation glide are enabled by the relatively high initial dislocation velocity and low density. The reasoning for the subsequent relaxation in the deviatoric stress, is due to a high rate of generation of mobile dislocations at sources of heterogeneous nucleation and multiplication, which enable a rise in rate of plastic deformation by a larger number of new dislocations traveling at lower velocity and therefore lower opposing stress. The second rise in material strength is caused by a sudden decrease in the rate of heterogeneous nucleation, in concert with a steadily increasing rate of immobilization, which ultimately hinders the continued rate of generation of mobile dislocations. Higher equivalent deviatoric stress is required for continued

glide motion of these mobile dislocations at higher velocities. Later, the effective strain-rate decreases sufficiently as the material tends to a hydrostatic state, and the deviatoric stress continuously decreases until it is insufficient for continued flow.

The standard deviation in the particle velocity curve (i.e., depicting the scatter due to the heterogeneous microstructure) in the present simulations arise entirely as a result of differences in orientation of the crystal aggregates relative to the propagation direction. These differences coming solely from the coupled deviatoric/volumetric terms and energy stored in the lattice associated with dislocation slip, result in differences in the impedance and permissible elastic and plastic rate of deformation. The relationship between the standard deviation in the DNS realizations are plotted against the equivalent deviatoric stress in **Figure 9**, to enable a discussion regarding the significance of this effect for different deformation regions during NPI.

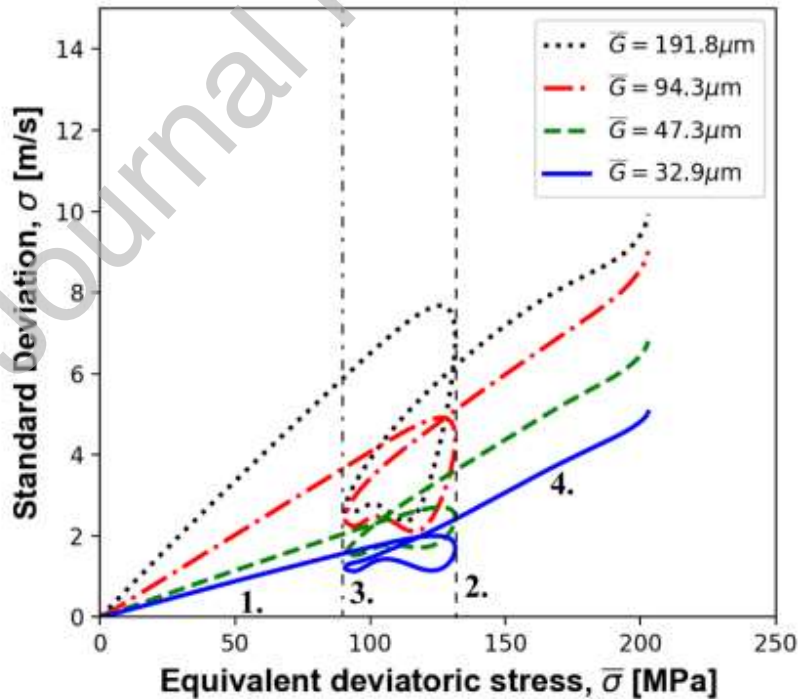


Fig 9. The standard deviation in the free surface particle velocity history for ensembles of each respective case of decreasing grain size versus the equivalent deviatoric stress in a comparable simulation employing our isotropic plasticity model.

Initially, in region 1 – 2, the standard deviation is proportional to the equivalent deviatoric stress, and the slope of the curve (i.e., the sensitivity of the scatter to deviatoric stress) increases with grain size. In this region, the scatter is primarily due to the differences in the elastic constants for different crystallographic orientations, resulting in the generation of elastic waves due to mismatching impedance and higher deviatoric stress levels at interfaces between grains due to the differences in their permissible rate of deformation. The relationship between the standard deviation with grain size can be explained physically by considering this to be a function of grains per area with favorable misorientation for near compatibility[72], therefore, one would expect that the deviatoric stress levels over a region of fixed size becomes more uniform when more grains are available.

In region 2 – 3 (i.e., corresponding to incipient plasticity) the standard deviation in the particle velocity decreases without much decrease in the deviatoric stress. This occurs because a significant portion of the total deformation gradient becomes accommodated by plastic deformation. Plastic deformation under these conditions is primarily governed by the rate at which crystals can deform plastically by the glide motion of geometrically permissible slip systems opposed by phonon drag. The relatively low standard deviation in this region is explained by the sufficiently large numbers of permissible slip systems and the stipulation of an initially uniform density of dislocations, which allows differently oriented crystals to accommodate plastic deformation by slip at similar rates and deviatoric stress levels. Consequently, the effect of grain size on the scatter is significantly reduced.

However, as plastic deformation continues (region 3 – 4), the standard deviation and differences in the curves due to the varying grain sizes re-emerges. The rise in standard deviation and the pronounced effect of grain size on the curves indicates that differently oriented grains are no longer able to accommodate plastic deformation at similar rates and deviatoric stress levels. We explain this effect by considering the role of grain size on the localization of the effective plastic strain (i.e., proportional to the total dislocation density).

3.1.2 The effect of grain size on the evolution of the effective plastic strain

At incipient stages of plasticity, (i.e., region 2 – 3) the sufficiently large numbers of permissible slip systems and the stipulation of an initially uniform density of dislocations, permits the uniaxial strain conditions imposed by the shock to be accommodated by differently oriented crystals without much variations in the stress, however, as plasticity continues we observe an increase in the variations in the stress. This is caused by an alteration in the initially uniform dislocation density promoting localization at regions of high deviatoric stress.

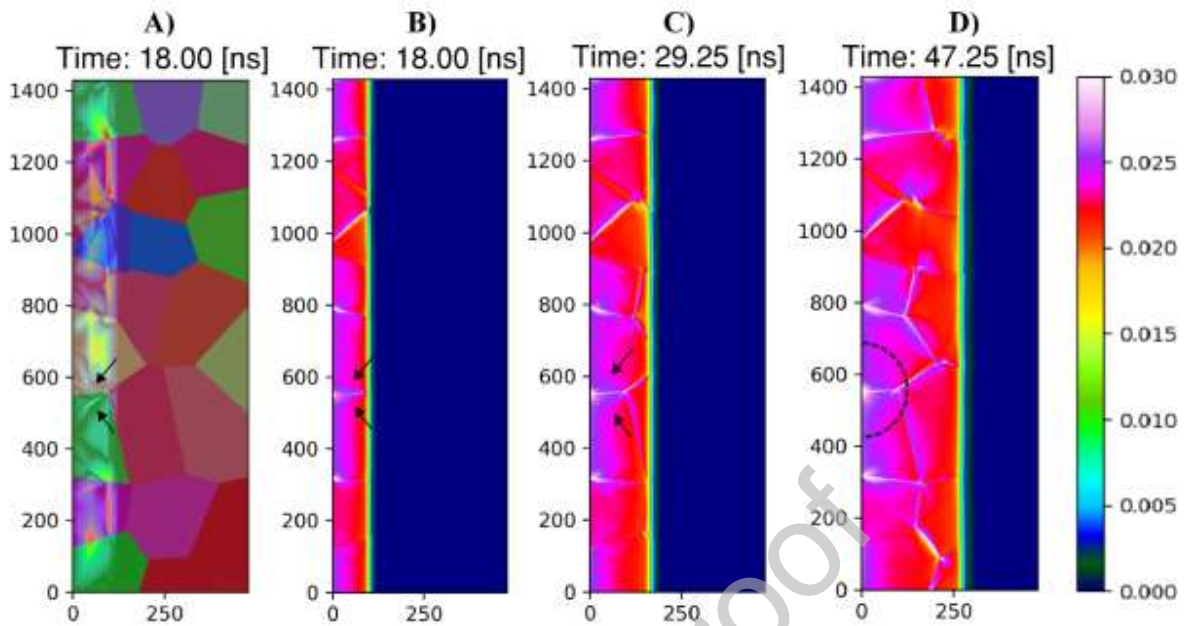


Fig 10. A) Shows the transverse particle record for an NPI simulation (Case A) at $t = 18$ ns after impact superimposed onto the microstructure geometry. The color map on the right of A) corresponds to the transverse particle velocity, whereas the color of the grains correspond to the colors on the standard IPF. B) – D) shows the evolution of the effective plastic strain in the mesh for the same simulation at increasing times.

In the present simulations, as the longitudinal wave propagates through the specimen, the differences in impedance and rate of deformation between neighboring grains cause regions of high deviatoric stress at the grain boundaries, resulting in i) a region of high localization of the effective plastic strain, and ii) the propagation of a re-compressive or release wave, which further modulates the strain fields within its reach. **Figure 10a)** shows the transverse particle velocity field (i.e. Y – component) superimposed onto the microstructure for a particular simulation of approximately $191.8 \mu\text{m}$ average grain size. Note that the colors of the grains correspond to the standard IPF, and the colors of the transverse particle velocity field correspond to the colormap to the right of A). **Figure 10 B-D)** shows the evolution of the effective plastic strain field as the

longitudinal wave propagates across the sample. The colors on this plot correspond to the colormap on the right of D). It can be observed in **Fig 10a**), that waves having transverse particle velocity components are generated at multiple grain boundaries bisecting the wavefront forming chevron like patterns pointing towards the instantaneous origin. For viewing convenience, we mark the evolution of the wave front of a particular wave by black arrows. **Fig 10 B) – D)** shows an enhanced effective plastic strain in regions for which this wave has traversed. We believe that the effect of grain size in the localization of various state variables and in the generation, propagation and interaction of these re-compressive and/or release waves can explain the scatter in the present simulations.

As an example, we plot the transverse particle velocity and effective plastic strain fields in a representative case for each average grain size in **Figure 11**. **Fig 11 A-D)** shows the effect of grain size on the resulting magnitude of the transverse particle velocity and effective plastic strain fields at the time of arrival of the longitudinal wave at the free surface. It can be clearly seen that the regions depicting a high magnitude in transverse particle velocity and low effective plastic strain are reduced in size with decreasing average grain size. The net effect is a more homogeneous strain and particle velocity field with decreasing grain size. This occurs because regions of the grains interior to the grain boundaries become more proximate to the grain boundaries, hence, re-compressive and release waves generated at grain boundaries are able to reach the entire grain, resulting in more uniform intra-granular distribution of various state variables. Additionally, the decreasing grain size seems to restrict the areas of intergranular fluctuations in the state variables to regions proportional to the average grain size.

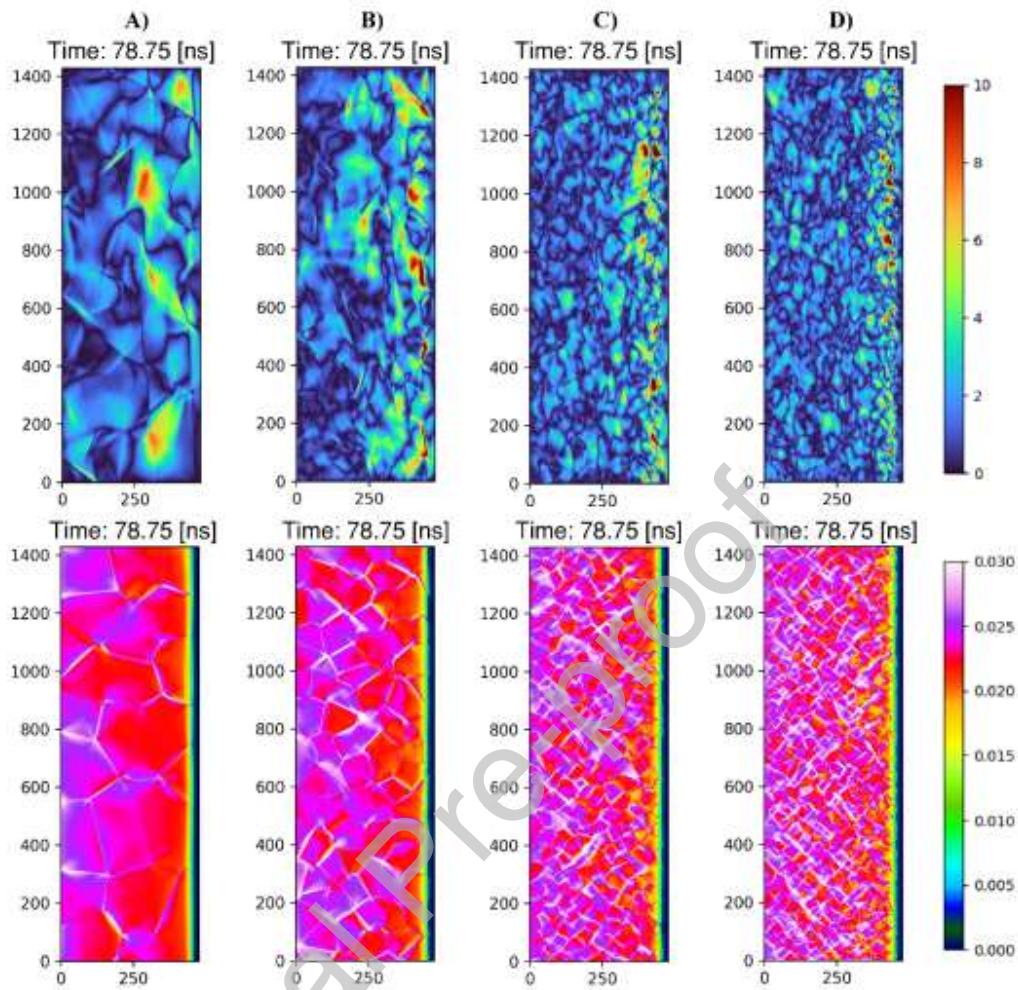


Fig 11. Shows the effect of grain size on the resulting magnitude of the transverse particle velocity and effective plastic strain fields at the time of arrival of the longitudinal wave at the free surface. It can be clearly seen that the regions depicting a high magnitude in transverse particle velocity and low effective plastic strain are reduced in size with decreasing average grain size.

3.1.3 Criteria for obtaining a representative value at the HEL from point measurements

An important application of the present DNS results is that they may be used in generation of a criteria for obtaining representative values from key locations in point measurements. As an example, we perform an analysis of the upper and lower values of the HEL. The mean value of the upper and lower HEL and the corresponding CV are plotted in **Figure 12**. Here, the upper

value of the HEL is denoted by a cross, and the lower value of the HEL is denoted by a filled circle. **Fig 12a)** shows that the ensemble average of the upper and lower values of the HEL are nearly identical in the range of simulated grain sizes. Moreover, the CV at the upper and lower values of the HEL decrease monotonically from 7 % and 9 % to 3 % and 4 % as grain size is reduced from approximately 192 to 33 μm . The small differences in the mean values and decreasing CV allow us to conclude that at smaller average grain size, the CV is expected to converge to zero, coincidentally the upper and lower HEL values are expected to converge to their respective mean-field value. In order to demonstrate this asymptotic convergent behavior, we assume a power-law form to describe CV versus average grain size, i.e., $CV = CV_0 + \alpha G^p$, the power law fit to the simulated data is shown as red and black dashed curves in **Fig 12b**. The values of CV_0 , α , and p , were found to be -12.1, 10.7, 0.11, respectively, for the upper HEL values, and -18.9, 15.7, 0.11 for the lower HEL values. The results show that the random uniform distribution of grain orientations and equiaxed grains present within the synthetic microstructure geometry average the effects from local heterogeneity, such that, the point measurements are convergent to their respective mean-field values for small enough average grain sizes.

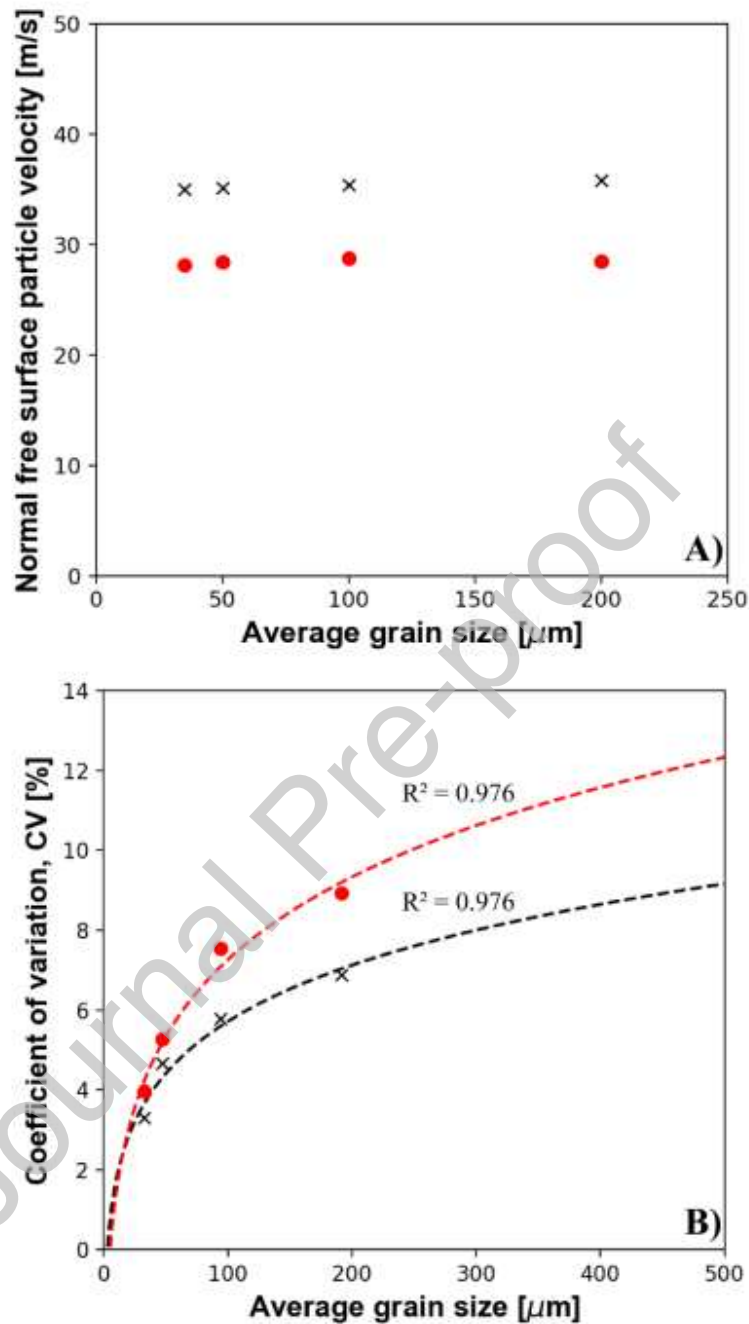


Fig 12. The mean **A)** and coefficient of variation, CV **B)** for the upper and lower values of the HEL all cases. Here the upper value of the HEL is denoted by a cross, and the lower value of the HEL is denoted by a filled circle. In **B)** the convergent behavior of the CV vs grain size is fitted to a power law asymptotic convergence. The estimated order of convergence, p , is approximately 0.11.

The minimum size for a representative element is often normalized by the characteristic length. For demonstrative purposes, we normalize the power law shown previously by dividing by the propagation length, , i.e. becoming $CV = CV_0 + x^p \alpha \left(\frac{x}{\bar{G}}\right)^{-p}$. Next, we plot the CV for the upper value of the HEL versus the normalized length, x/\bar{G} obtained from the same DNS simulations at range of propagation distances interior and on the free surface and compare this to the power law with the same parameters from those obtained in **Fig 12** (i.e. $x = 0.5$ mm), this is shown in **Figure 13**.

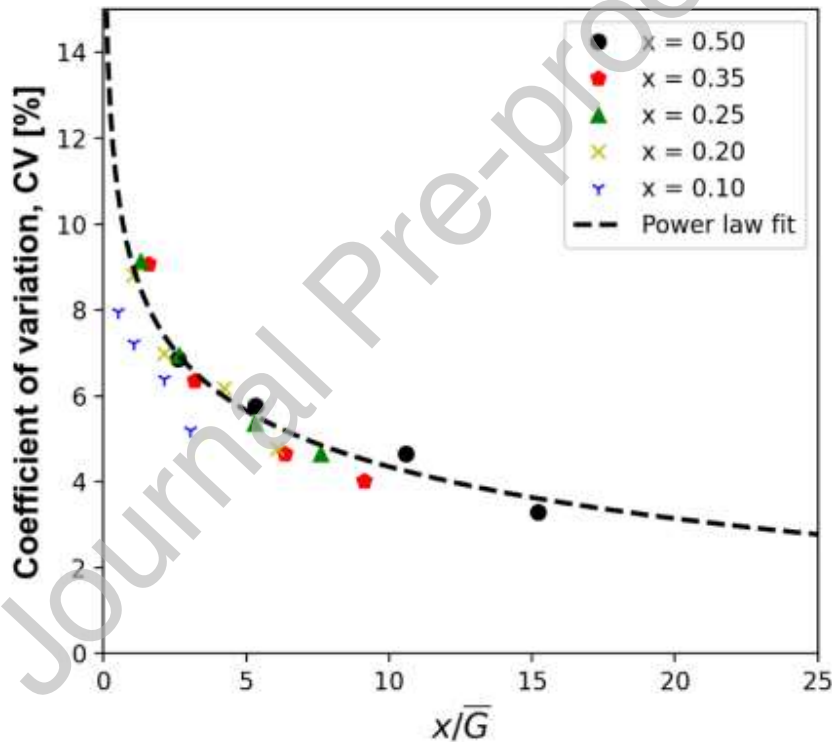


Fig 13. The CV versus the ratio between the propagation distance, x and the average grain size, \bar{G} for the upper value of the HEL at a range of propagation distances. The plot shows that the behavior of the CV versus normalized length for a wide range of propagation lengths fits the power law description.

Remarkably, the CV versus x/\bar{G} for a wide range of propagation distances (e.g. 0.2 – 0.5 mm) is observed to correlated well with the powerlaw description shown in the above. Demonstrating

that the powerlaw fit may be used as a criterion for designing an experiment to minimize CV. For example, using this, we calculate that for a CV of about 5% and 3%, the minimum required number of grains per propagation length is approximately 7-8, and 20-22, respectively. At smaller propagation distances of less than 0.2 mm, the CV is less than the predicted CV for larger propagation distances for the same x/\bar{G} . However, caution should be employed when using the same powerlaw fit in designing experiments of very short propagation distances because the presently employed material model was calibrated to experiments of between 0.1 – 2 mm. Hence, at smaller propagation distances, the results would reflect predictions rather than interpolations.

3.1.4 Comparison of DNS results to our isotropic plasticity model

The results suggest that point measurements in analogous NPI experiments involving polycrystalline aluminum can also be expected to demonstrate a convergent behavior towards a mean-field macroscale value. The DNS framework outlined in this section can be used to estimate the measurement uncertainties due to the material variability. For example, for experiments employing pure annealed polycrystalline aluminum [29, 73] with no preferential orientation and equiaxed grains we estimate uncertainty bounds by considering the distribution of the ensemble with a grain geometry similar to those employed in experiments. **Figure 14** superimposes the distribution of outcomes (of a 50-micron average grain size ensemble) against the predictions of our isotropic plasticity model [29].

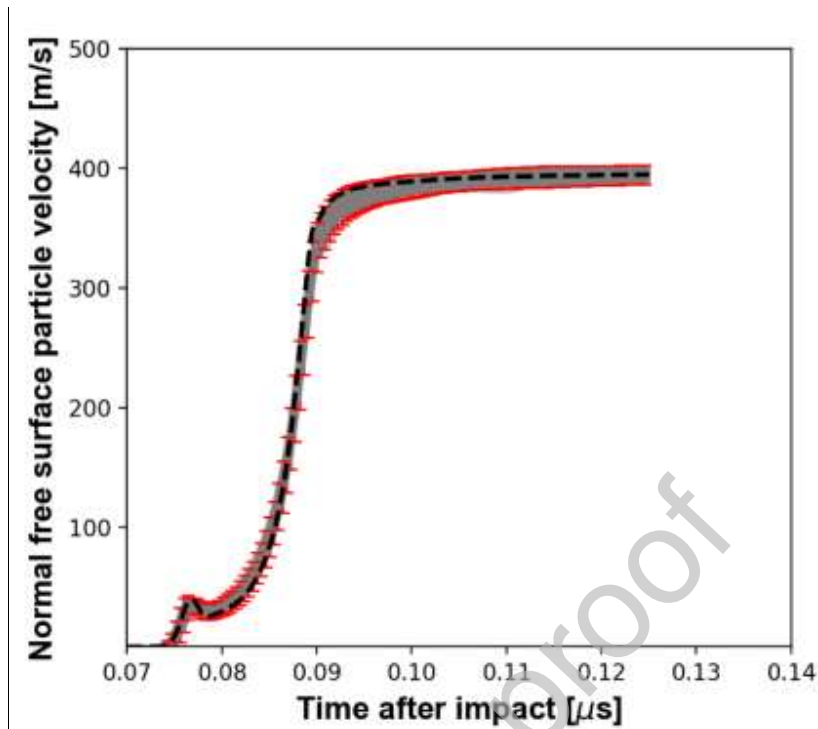


Fig 14. A comparison of simulation results using a macroscale, isotropic model with those from ensemble D containing equiaxed grains of average grain size of 50 μm . Shows the simulated free surface profiles from the ensemble (light gray curves) and the isotropic plasticity model from [17] (dashed). Also, shown are the mean of the ensemble with red error bars of approximately three times the standard deviation. The error bars are shown to closely envelop the realizations of the ensemble.

Fig 14 shows the realizations as light gray colored curves, against the deterministic simulation employing our isotropic model in the dashed black curve, moreover, we superimpose the mean of the ensemble with red error bars of approximately three times the standard deviation. This choice of error bars closely envelops all of the realizations in the ensemble. These results characterize possible deviations of any single microstructure realization from the true ensemble average response, which highlights the need for careful consideration when fitting an isotropic model to the measurements from a single realization or experimental shot. In other words, given a finite specimen size and characteristic grain size, the corresponding experiments would be expected to exhibit variability on the same order of magnitude (or larger) as these microstructure

simulation results, thus, results from any specific experimental shot may be biased away from a representative macroscale behavior. For the grain sizes considered, the upper and lower values of the HEL of a single realization can deviate from the mean by up to about 12% (approximately three standard deviations). However, the NPI experiments [73] considered when calibrating the isotropic model involved samples with a finer average grain size of approximately 10 μm . At these fine grain sizes, the deviation from the true mean in the measurements will likely become limited by errors in the experimental method and diagnostics involved rather than by microstructural heterogeneity. An estimate of the CV for a 10-micron average grain size yields a value of less than 2% for the upper and lower HEL values at the 0.5 mm and even lower for larger propagation distances, hence, we expect there to be good agreement between an isotropic model and NPI experiments.

3.2 Combined compression-shear of synthetic polycrystalline aluminum

In PSPI experiments, the oblique impact of a foil sample between two anvil plates results in the propagation of longitudinal and transverse wave modes. Moreover, the thickness of the sample is chosen such that the normal stress quickly rings up in the specimen and reaches a nearly uniform hydrostatic state within a few reverberations of the longitudinal wave (i.e., after the ring up period). The high compressive stresses enable the anvil/sample interfaces to support considerable shear stress through contact friction [74]. The shear stress in the specimen also quickly rings up, resulting in the uniform shearing deformation of the sandwiched sample under combined compression shear. The subject of our past study [29] has been to determine the dynamic shearing resistance of polycrystalline aluminum at large values of strain. For PSPI experiments involving polycrystalline specimens, although the entire specimen is subjected to uniform shearing deformation through its thickness, it is unclear if the point measurements at the free surface are representative of the macroscopic deformation of the sample. This concern is exacerbated in PSPI experiments since the samples are thin and often only contain a single grain through its thickness but multiple grains along their radial dimensions, as illustrated in **Fig 4b**. This question serves as one primary motivation for the present investigation. Hence, the present PSPI simulations are designed primarily to reveal if the transverse particle velocity history demonstrates a convergent behavior towards a mean-field value as the grain size is reduced along the shearing direction.

For the PSPI series, the IPFs for cases A through E are provided in **Figure 15**. Similarly, to the previous DNS case, the position of a point on the IPF reveals the alignment of the respective crystallographic direction of the grains to the global X-direction and indicates that there is no

preferred orientation for grains. In contrast to the previous case, our estimate of the grain size, G , corresponds to a one-dimensional length of a grain along the shearing direction (i.e., the global y-direction). This is because of the limited 50 μm specimen thickness, which limits the size of the grains along the global X-direction. The approximate one-dimensional grain size for cases A, B, C, D, E are found to be about $1758 \pm 1037 \mu\text{m}$, $440 \pm 256 \mu\text{m}$, $277 \pm 156 \mu\text{m}$, $175 \pm 93 \mu\text{m}$, $117 \pm 62 \mu\text{m}$, respectively.

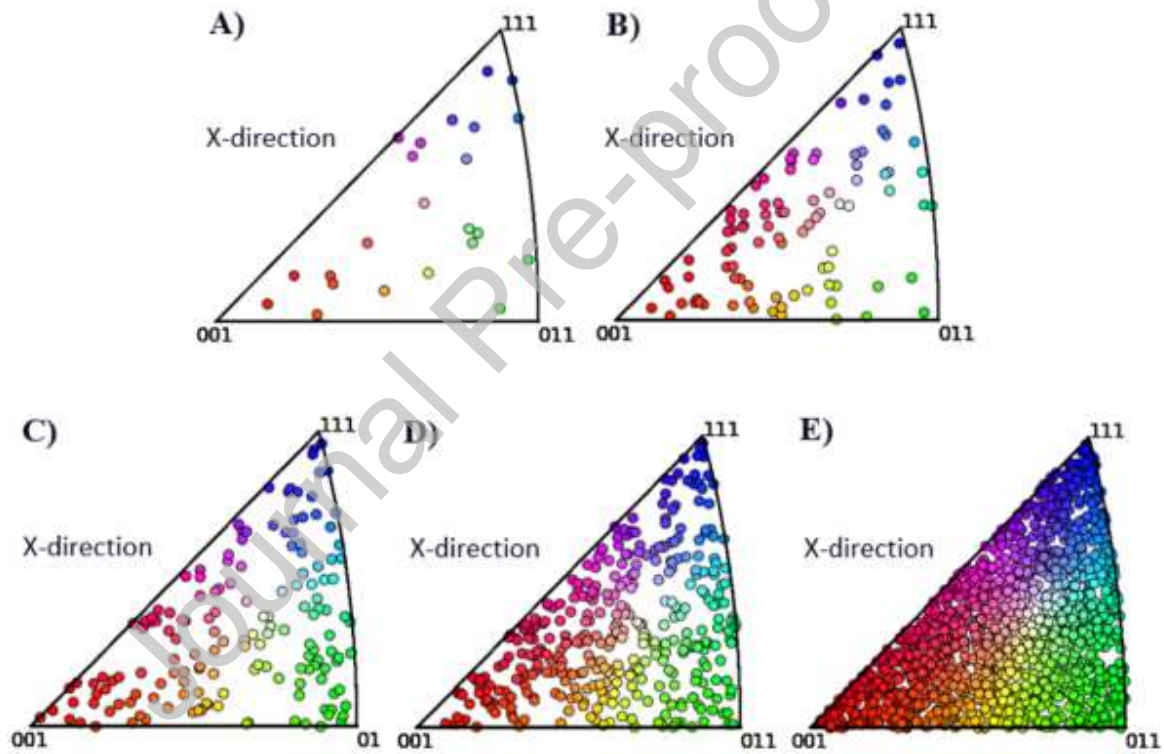


Fig 15. The inverse pole figures for the four simulation cases employing the PSPI series. The average grain sizes for case A, B, C, D, and E are 1758 μm , 440 μm , 277 μm , 175 μm , 117 μm , respectively. The position of the point on the IPF reveal the alignment of the respective crystallographic direction of the grain to the global X-direction. Moreover, the IPF shows that the micrograph displays no texture in all cases.

3.2.1 The effect of grain size on dispersion in the transverse particle velocity history

The transverse particle velocity records at the center of the free surface (i.e., at the red circle in the **Fig 4b**) for all cases are presented in **Figure 16**.

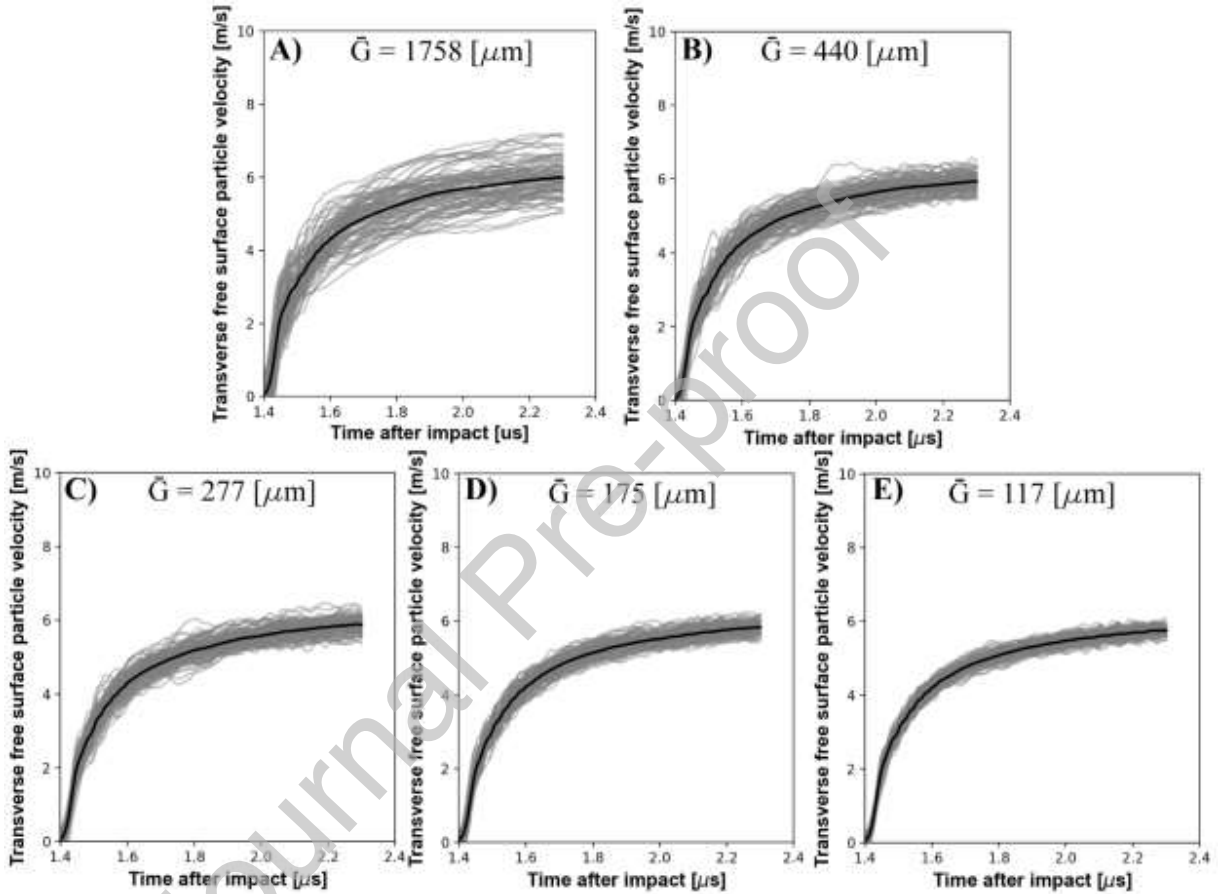


Fig 16. Transverse particle velocity history at the center of the free surface of the sample ($X = L$, $Y = 0.5D$) for each case **A-E** in the PSPI series. The semi-transparent colored curves represent individual realizations for each case and the solid black curve is the average of the ensemble of simulations for the respective case.

The gray curves represent individual realizations, and the solid black curve represents the average of the ensemble. In every simulation, the transverse particle velocity history shows an initial gradual rise in particle velocity, which is mostly governed by the elastic response as the

shear stress in the specimen rings up until it exceeds the flow stress. Subsequently, the plot shows a more gradual rise in particle velocity, which is governed by the strain hardening in the plastic deformation regime. **Fig 16** shows noticeable variations in the particle velocity record at all times after the arrival of the transverse wave. The magnitude of these variations and how they change with successive grain refinement (from case A through E) are generally consistent with the series of NPI microstructure simulations. It can be clearly seen that the magnitude of the variations in the transverse particle velocity record decrease with decreasing grain size. In PSPI configurations, our particular interest is in the variations after the ring-up period, which have been reported to last less than 100 ns in analogous experiments employing pure polycrystalline aluminum [29].

The mean and CV for the ensemble of simulations versus time are plotted in **Figure 17**. **Fig 17a** shows that the mean of the ensemble is nearly identical in the range of simulated grain sizes, exhibiting negligible changes in the magnitude of the flow stress and strain hardening at higher levels of strain. And again, **Fig 17b** shows that the CV monotonically decreases from case A to E (i.e., with grain refinement). The time dependence of the CV is also generally consistent with the case of NPI, decreasing with time reaching the smallest value at the end of the simulation window. The CV of the transverse free surface particle velocity history, after the ring-up period, decreases from approximately 12 - 9 % to 2 - 1 % when the approximate grain size along the shearing direction is reduced from about 1758 μm to 117 μm . At smaller average grain size, the CV is expected to converge to zero, such that point measurements of transverse free surface particle velocity are expected to converge to their respective mean-field value. However, the reasoning for this decrease is unique to PSPI.

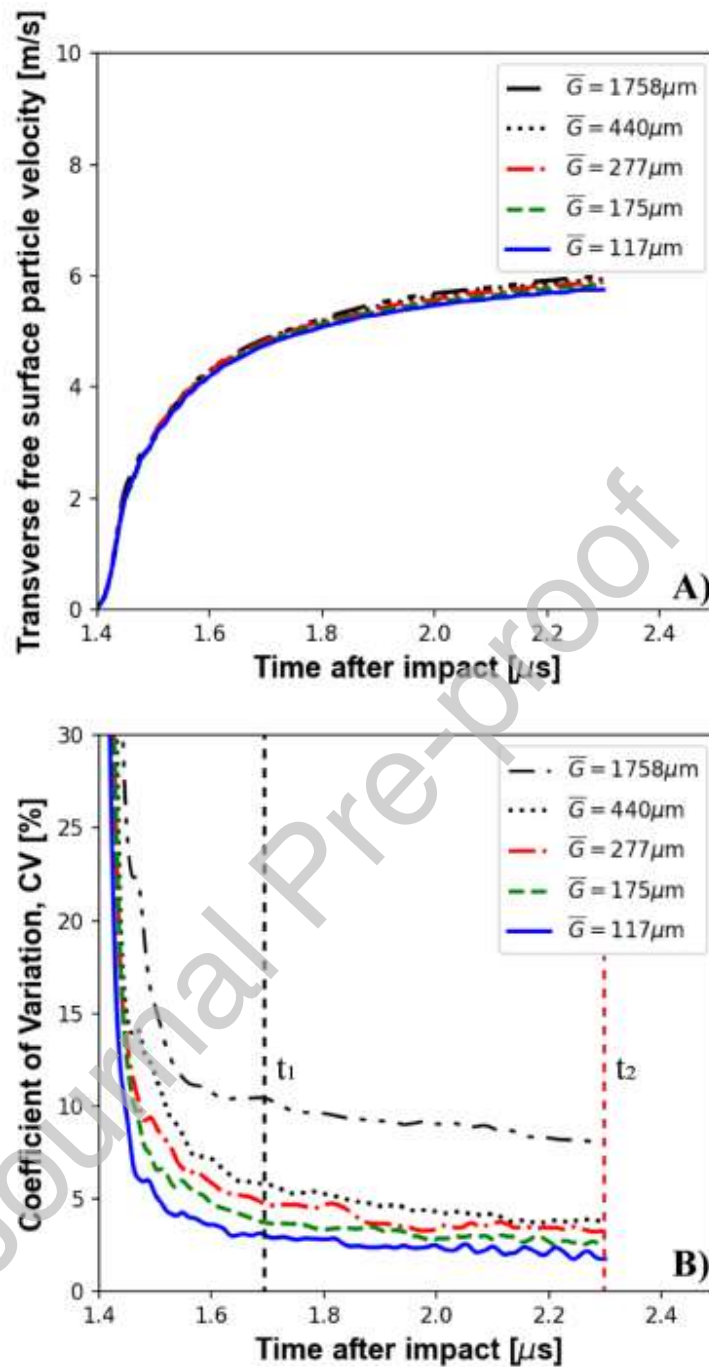


Fig 17. The mean **A)** and coefficient of variation **B)** (i.e., the ratio between the standard deviation and the mean) for the ensemble of simulations of each case versus time after impact. **A)** shows that the mean for all cases is nearly identical, with its largest difference (of less than 1%) being just prior to the shock plateau. **B)** Shows that the CV decreases with successively with decreasing grain size.

The standard deviation, σ of the transverse particle velocity with time (i.e., depicting the scatter due to the heterogeneous microstructure) is plotted in **Fig 18**. As mentioned in the above, in the first hundred nanoseconds, the deviatoric stress in the specimen is ringing-up. The initially high and/or oscillatory standard deviation early in time is attributed to this the ring-up period. After the ring-up period, the standard deviation is observed to remain relatively constant throughout the experimental window. This accords well with the previous observations that the standard deviation is proportional to the deviatoric stress level, since these levels are also nearly constant throughout the PSPI experiment. Hence, the decrease in the CV with time is primarily attributed to the decreasing ratio of the constant standard deviation with increasing mean transverse free surface particle velocity.

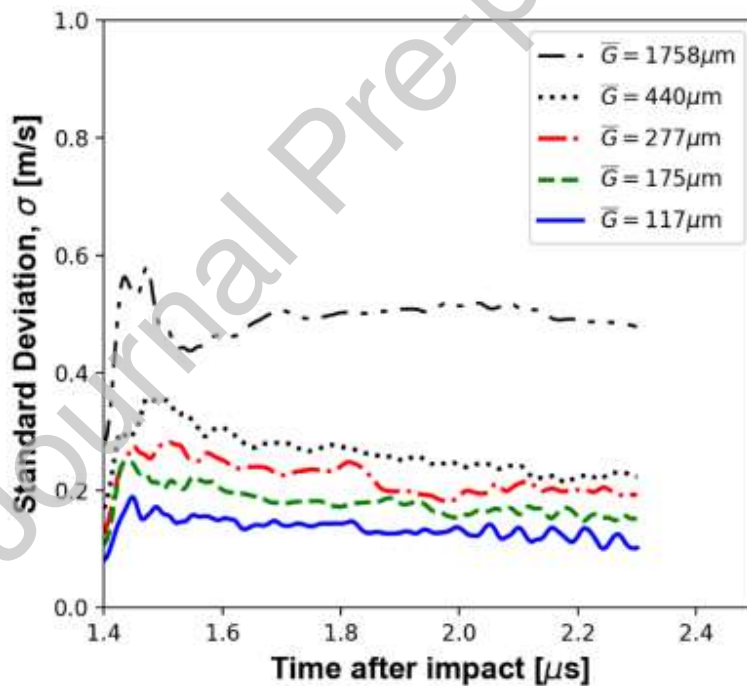


Fig 18. The standard deviation in the transverse free surface particle velocity history for ensembles of each respective case of decreasing grain size.

The reasoning for the effect of average grain size on the observed scatter in the DNS realizations are again explained within the context of dislocation glide kinetics. However, the mechanisms

contributing to dislocation glide are limited by thermally-assisted glide passed short-range obstacles rather than hindered by phonon drag. This has been described in detail in our previous work, and is owed primarily to the much higher levels of effective plastic strains (i.e. higher dislocation density) achieved quickly in PSPI, which enhance the mechanical threshold stress associated with short-range barriers by the Taylor hardening relationship [29]. Under these conditions, the main differences in the rate of deformation of crystals of different crystallographic orientations are owed to the critically resolved shear stress on the permissible slip systems. The anisotropy in the response of the crystals are expected to be initially low, however, quickly rises due to the preferential accumulation of dislocations in regions of high deviatoric stress (i.e. grain boundaries) due to the differences in the permissible shearing rate for differently oriented crystals. The decrease in the grain size reduces the scatter in the shearing resistance of the polycrystalline specimen, by the generation of shearing and release waves at grain boundaries, which result in more uniform intragranular distribution of state variables (i.e. stress, particle velocity) and restrict the fluctuations in the intergranular variable fields proportionally to the scale of the grains. It is also possible to discuss the effect of pressure in the context of the present model. Increasing hydrostatic pressure would likely only play a limited role on the scatter in these experiments, since the compressive wave quickly rings up and the plastic deformation associated with compression is orders smaller than that caused by in-plane shearing. Moreover, even though hydrostatic pressure could have a pronounced effect on the dynamic shearing resistance, the pressure dependence of the effective elastic constants in the present model would increase the shearing resistance proportionally for different crystallographic orientations, hence, this would not affect the CV.

3.2.2 Criteria for obtaining a representative measurements of shearing resistance from point measurements

In order to create a criteria for obtaining a representative measurements of shearing resistance from point measurements, we again assume a power-law form to describe CV versus average grain size. The power law fits to the simulated data at $t_1 = 1.7 \mu\text{s}$ and $t_2 = 2.3 \mu\text{s}$ are shown in **Figure 19** as black and red dashed curves, respectively. The values of α , and p , were found to be 0.375, 0.445, at t_1 , and 0.1711, 0.514 at t_2 , and the values of CV_0 were negligible. For PSPI, we do not normalize the grain size by a characteristic length, but provide guidance by specifying the grain size rather than the number of grains per characteristic length. E.g., if the desired CV is below 3%, the average grain size should be below about 100 microns.

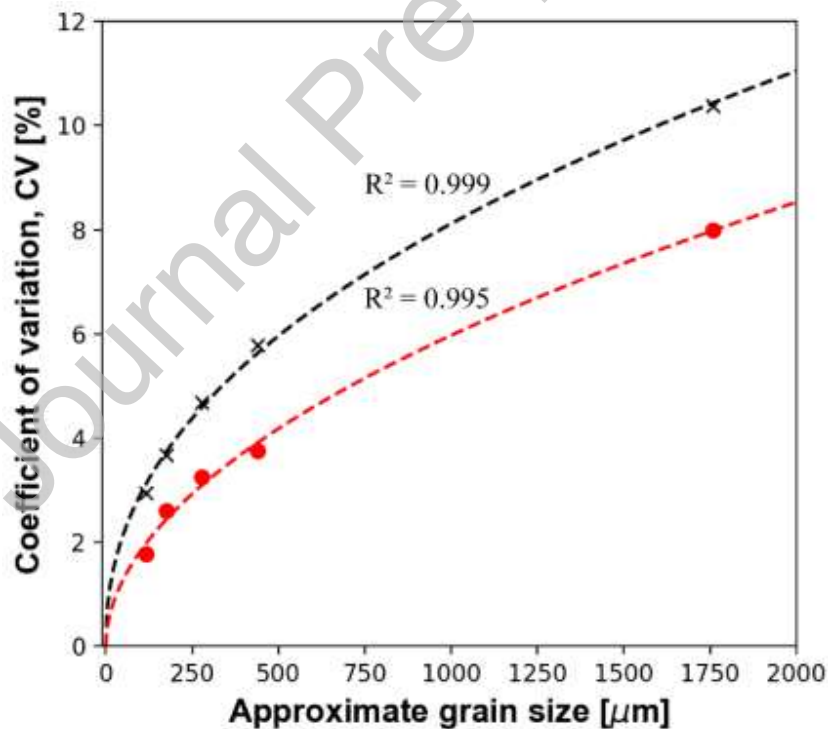


Figure 19. Shows a power law fit to the simulated coefficient of variation at times $t_1 = 1.7 \mu\text{s}$ and $t_2 = 2.3 \mu\text{s}$.

3.2.3 Comparison of DNS results to our isotropic plasticity model and discussion of the implications of finite specimen size in PSPI experiments

An important result from the present DNS simulations, is that the point measurements in PSPI are indeed expected to be convergent to their respective mean-field values for small enough grain sizes along their lateral dimensions (i.e., as more grains become available along the shearing direction) despite only containing a single or few grains through thickness. The assumption that a PSPI experiment employing a limited specimen size with few grains through thickness could recover the representative response of a polycrystalline metal had not yet been validated in the literature until now. However, the uncertainties involved motivate a discussion regarding the implications of making inferences of dynamic shearing resistance from single point velocity measurement.

The DNS framework outlined in this section can be used to simulate the variance due to the grain geometry in the context of a typical PSPI experiment. For example, we provide an estimate for the uncertainty bounds in our previous PSPI investigation [29] by considering the grain size of the sample employed. **Figure 20** superimposes the distribution of outcomes (of Case C employing 250-micron average grain size) against a simulation of our isotropic plasticity model [19], which has been calibrated to experiments employing approximately 150 – 200-micron grain size. **Figure 20** shows the realizations in light gray colored curves along with previously reported [29] simulation results from the isotropic macroscale model represented by the dashed black curve. The results characterize the possible deviation of any single microstructure realization (analogous to a single experiment) from the true ensemble average response. In other words, given a finite specimen size and characteristic grain size, the corresponding experiments would be expected to exhibit variability on the same order of magnitude (or larger) as these

microstructure simulation results, thus, results from any specific experimental shot may be biased away from a representative macroscale behavior.

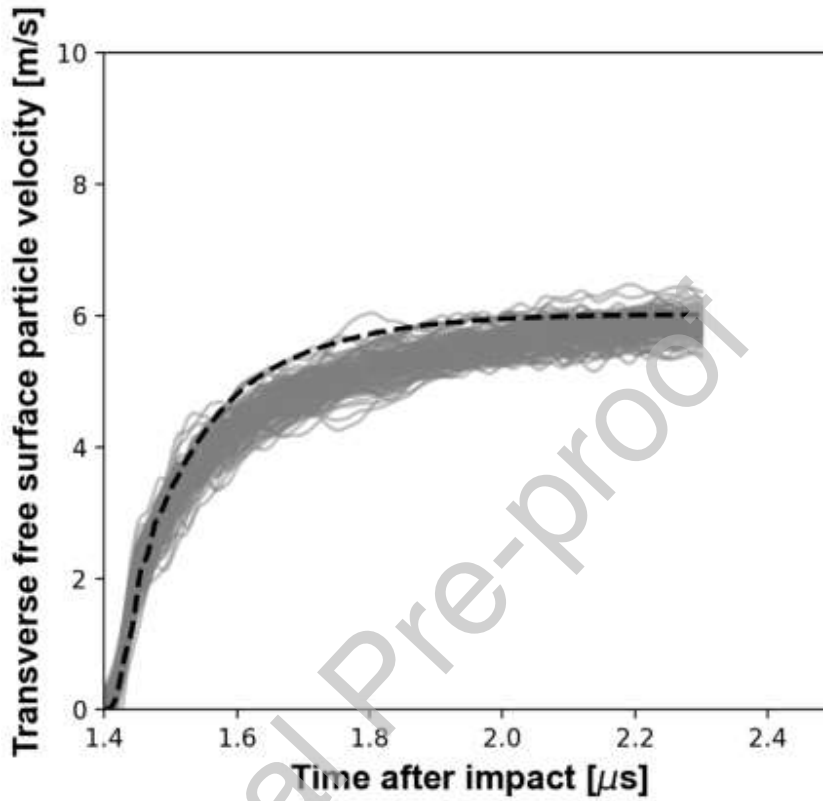


Figure 20. Comparison of the macroscale model results and those from ensemble C containing equiaxed grains with average grain size of $277 \mu\text{m}$. shows the simulated free surface velocity profiles from the ensemble (gray) in comparison to results from the isotropic plasticity model from [29] (dashed).

Although there is adequate agreement between the simulations in that the isotropic plasticity model lies within range of possible realizations from DNS, these results highlight the need for careful consideration when fitting an isotropic model to a single shot employing finite specimen size and a polycrystalline geometry. This is illustrated by the deviation of the isotropic model from the true mean of the ensemble in **Fig 20**. To further illustrate the possible bias of any

specific experimental shot from the representative macroscale behavior (i.e., the mean of the ensemble), we provide some examples in **Fig 21** showing the possible deviation of individual realizations from the mean of the ensemble due to the local grain geometry.

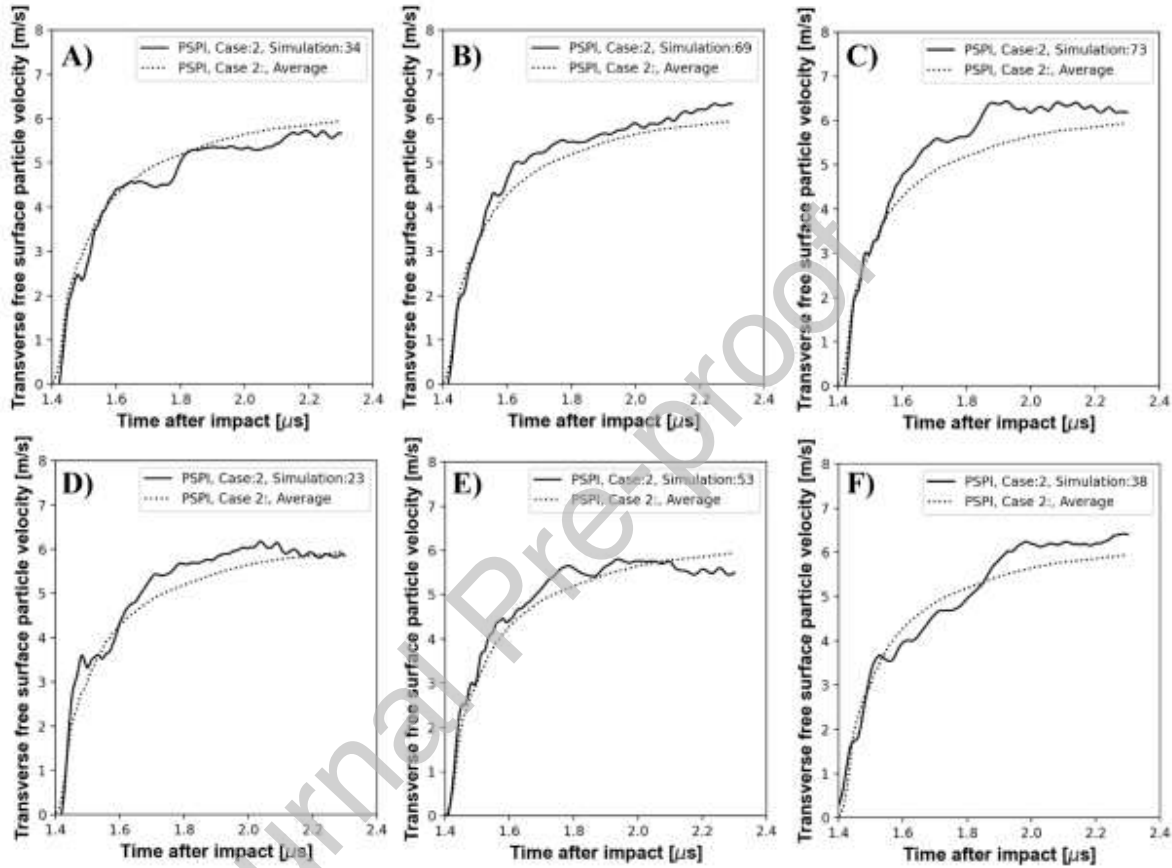


Fig 21. Illustrates the possible bias of any specific experimental shot from the representative macroscale behavior (i.e., the mean of the ensemble), showing a range of possible deviations of individual realizations from the mean of the ensemble due to the local grain geometry.

Figures 21 A) – C) show scenarios in which the strain hardening behavior of a single realization may significantly differ from the expected mean response, e.g., A) shows abrupt changes in the strain hardening occurring at discrete time intervals, B) exhibits a response similar to a bilinear hardening, and C) initially overshoots the flow stress and then subsequently plateaus and softens,

whereas the mean response is expected to gradually soften with increasing plastic strains. Moreover, D) – F) show that the level of the flow stress of a single realization may initially overshoot or undershoot the mean response and later reverse. e.g., E) initially overshoots the flow stress of the mean response but softens quickly and later falls below the expected mean response, while F) initially undershoots the flow stress, but later quickly hardens and overshoots the flow stress at larger plastic strains.

The results demonstrate that the transverse particle velocity history in PSPI experiments with a single grain through thickness but several grains along the shearing direction shows a convergent behavior towards a single mean-field value for the typical range of specimen dimensions and grain sizes. However, careful considerations must be taken when interpreting the results and calibrating isotropic plasticity models, because individual realizations will likely exhibit variability due to the local grain geometry that significantly differ from the expected mean response. The extent to which an individual realization may differ from the mean response is expected to decrease with decreasing average grain size, hence, if the grain size is further refined, such as in Case E, the transverse particle velocity record can be expected to deviate from the mean by only a few percent. In these cases, involving fine grain sizes, the deviation from the true mean in the measurements will likely be limited by errors in the experimental method and the diagnostics rather than by microstructural heterogeneity.

One primary motivation of the present work was to investigate the source of localized fluctuations in the particle velocity record that were observed experimentally in our previous PSPI experiments [29], but were not reproduced numerically. Based on the results from the present DNS, we conclude these fluctuations in particle velocity were likely due to the effects of

the heterogeneous microstructure, which were not captured in the isotropic plasticity model. An interesting avenue of future work would be to use a laser diagnostic capable of measuring dispersion in the transverse particle velocity record similar that of Asay and Barker [34] for the normal particle velocity, which could then be compared to DNS simulations and allow for a more thorough investigation on the effect of the heterogeneous microstructure. Certainly, this type of investigation can already be conducted for the case of NPI, and will be the subject of our future work. This will provide crucial validation for the present DNS framework for minimizing scatter in NPI and PSPI experiments.

4. CONCLUDING REMARKS

In summary, we employed a continuum crystalline plasticity model to perform direct numerical simulations (DNS) of statistically representative microstructures of polycrystalline aluminum within experimental specimens subjected to dynamic compression and compression-shear loading. Our aim was to study the magnitude of variations of point measurements in dynamic experiments on polycrystalline aluminum involving a finite specimen size, where the source of the scatter due to the polycrystalline microstructure was a result of grain-to-grain differences in size and crystallographic orientation. Two series of simulations were carried out and are reported (i.e., one series for NPI and for PSPI, respectively). For each series, there were several simulation cases (A-D for NPI, and A-E for PSPI) containing an ensemble of one-hundred realizations per case. Each case had a different average grain size, which was refined successively with increasing alphabetical order. Each simulation employed a different randomly generated microstructure geometry and associated random uniform distribution of grain size and orientations.

The results from DNS revealed that in both loading configurations, the mean response of the ensemble was nearly coincident for the range of simulated grain sizes. Moreover, the grain size directly correlated with the coefficient of variation in the expected point measurements, i.e. in the dispersion of the normal and transverse free surface particle velocity history, showing a monotonic decrease as the sample grain size was reduced. These findings suggested that the point measurements have a convergent behavior toward the ensemble average value. The magnitude and significance of the scatter in the particle velocity record was shown to be largest where the deviatoric stresses were most significant, also suggesting that the effect would

decrease in significance at very high hydrostatic pressures. In the case of NPI, this occurred at the elastic and plastic wavefront, whereas, in the case of PSPI, the magnitude of fluctuations were approximately constant throughout the experimental window time. The main reasoning for the scatter was identified as being due to varying deviatoric stress levels arising from differences in the permissible rate of deformation of grains with varying orientation with respect to the loading configuration. The net effect was a localization of the elastic and plastic strain at the grain boundaries, resulting in inter and intra-granular variations in the distribution of several pertinent variable fields. The decreasing grain size limited the regions of fluctuations in the distribution of states variables proportionally with the average grain size.

In the case of normal shock compression simulations, after propagating over one millimeter, the CV of the elastic precursor amplitude was observed to monotonically decrease from approximately 7 and 9 % to 3 and 4 % (for upper and lower values of the HEL) when the grain size was reduced from 192 μm down to 33 μm . An important result of the DNS simulations was that the decrease in CV versus normalized length (i.e., propagation distance by average grain size) for a range of propagation distances between 0.2 – 0.5 mm was shown to fit well to a powerlaw form. We concluded that this powerlaw could be used in designing NPI experiments involving polycrystalline aluminum for minimizing dispersion in the normal particle velocity record. In combined pressure-shear dynamic loading, the CV, after an initial ring-up period, the transverse free surface particle velocity history was shown to decrease from approximately 12 - 9 % to 2 - 1 % as the average grain size (along the shearing or global Y-direction) was reduced from about 1758 μm down to 117 μm . The decrease in the CV with grain size was also shown to fit well to a powerlaw. For these reasons, it was concluded that at smaller average grain size, the CV is expected to converge to zero and point measurements of normal and transverse particle

velocity history are expected to converge to their respective mean-field value if the grain size is sufficiently small. It should be noted, however, that in the limit of small grain sizes (e.g. in nanocrystalline materials), other hardening effects (e.g. grain boundary strengthening) may eventually begin to dominate the response. The mean-field response of such materials may no longer be comparable to the mean-field response of the same material with larger average grain size. Hence, one important consideration in the analysis for determining the appropriate size for a representative measurement is the comparison between the predicted ensemble averages. The convergence analysis will only be valid in the range of grain sizes for which the mean response is approximately coincident.

Finally, the results from DNS were summarized into a framework for assessing the variance due to grain geometry in the context of typical NPI and PSPI simulations. The realizations from DNS were compared to simulation results using a previously developed dislocation kinetics-based isotropic plasticity model [29]. The goal of this comparison was to ascertain the limits of agreement that could be reasonably expected between the isotropic model, which does not account for grain scale heterogeneity associated with crystal orientations and local anisotropy, versus dynamic experiments with a finite specimen size. The main conclusions from this analysis included:

- The limits on what constitutes reasonable agreement between experimental measurements and isotropic models depends upon grain size with respect to specimen size.
- Careful consideration is required when using such experiments to develop and calibrate isotropic plasticity models, because individual realizations (e.g., individual experiments)

will likely exhibit variability due to the local grain geometry that may bias the observed response away from a representative macroscale behavior.

- The agreement between the two is expected to improve if a sufficient number of grains is available. Moreover, the experiments should be carefully designed in accordance to the present DNS framework for minimizing dispersion in the particle velocity history.
- The CV in NPI and PSPI experiments can be estimated using the powerlaw description provided by the present DNS framework.

ACKNOWLEDGMENTS

The authors acknowledge the support of Los Alamos National Laboratory operated by Triad National Security, LLC for the U.S. Department of Energy under contract 89233218CNA000001. In particular, the theory and modeling scope was supported by the Laboratory Directed Research and Development Program Director's Funded Postdoctoral Fellowship, LDRD 20190639PRD2, to Bryan Zuanetti at LANL. The authors would also like to thank Dr. Vikas Prakash from the Institute of Shock Physics at Washington State University for useful discussions related to this manuscript.

APPENDIX A. SUMMARY OF THE THERMOELASTIC MATERIAL DESCRIPTION

Kinematics

Following the arguments from Luscher et al. [75], the deformation gradient is multiplicatively decomposed by

$$\mathbf{F} = \mathbf{F}_e \mathbf{F}_p \# (\text{A.1})$$

where \mathbf{F}_p is the typical plastic part of the deformation gradient associated with crystallographic slip, and the elastic deformation gradient, \mathbf{F}_e , is further decomposed into volumetric and isochoric parts (i.e., $\mathbf{F}_e = \widehat{\mathbf{F}}_e \overline{\mathbf{F}}_e$). The volumetric part of the deformation gradient, $\overline{\mathbf{F}}_e$, is given by $\overline{\mathbf{F}}_e = J_e^{1/3} \mathbf{I}$, where J_e is the determinant of the deformation gradient.

The Green-Lagrange, and the isochoric and volumetric measures of the Green-Lagrange are given by

$$\mathbf{E}_e = \frac{1}{2} (\mathbf{C}_e - \mathbf{I}) \# (\text{A.2})$$

$$\widehat{\mathbf{E}}_e = \frac{1}{2} (\widehat{\mathbf{C}}_e - \mathbf{I}) \# (\text{A.3})$$

$$\overline{\mathbf{E}}_e = \frac{1}{2} \left(J_e^{2/3} - 1 \right) \mathbf{I} = \frac{1}{3} \delta \mathbf{I} \# (\text{A.4})$$

The isochoric Green-Lagrange strain defined with respect to the reference configuration is given by the volumetric pull-back of $\widehat{\mathbf{E}}_e$ by $\overline{\mathbf{F}}_e$ (i.e., $\widehat{\mathbf{E}}_e = \overline{\mathbf{F}}_e^T \widehat{\mathbf{E}}_e \overline{\mathbf{F}}_e$) facilitating the additive

decomposition of the total elastic Green-Lagrange strain with respect to the reference configuration (i.e., $\mathbf{E}_e = \bar{\mathbf{E}}_e + \hat{\mathbf{E}}_e$).

The pull back of the spatial gradient of the velocity field to the intermediate configuration can be expressed as $\tilde{\mathbf{L}} = \mathbf{F}_e^{-1} \mathbf{L} \mathbf{F}_e$, where $\mathbf{L} = \mathbf{v} \bar{\mathbf{V}} = \dot{\mathbf{F}} \mathbf{F}^{-1}$, is the spatial velocity gradient. Hence,

$$\tilde{\mathbf{L}} = \underbrace{\mathbf{F}_e^{-1} \dot{\mathbf{F}}_e}_{\tilde{\mathbf{L}}_e} + \underbrace{\dot{\mathbf{F}}_p \mathbf{F}_p^{-1}}_{\tilde{\mathbf{L}}_p}.$$

Thermodynamics

The nonlinear thermoelastic Helmholtz free energy, $\psi = \psi(\mathbf{E}_e, T, \xi)$, is defined as a state function of the Green-Lagrange strain, \mathbf{E}_e , temperature T , and internal state variables, ξ , representing the several aspects of dislocation population from the single crystal plasticity model, leading to the typical thermodynamic state relations (i.e.,

$\tilde{\mathbf{S}} = \tilde{\rho} \frac{\partial \psi}{\partial \mathbf{E}_e}$, $\eta = -\frac{\partial \psi}{\partial T}$, $\mathbf{f} = \tilde{\rho} \frac{\partial \psi}{\partial \xi}$) where $\tilde{\mathbf{S}}$ is the stress measure in the intermediate configuration, η is the entropy per unit mass, \mathbf{f} represents stress-like terms conjugate to the microstructural state variables, and the density $\tilde{\rho}$ in the intermediate configuration.

We decompose the Helmholtz free energy into

$$\psi(\mathbf{E}_e, T, \xi) = \hat{\Psi}_{\text{nonlin}}(\mathbf{E}_e, T) + \hat{\psi}_{\text{str}}(\xi) \quad (\text{A. 5})$$

where $\hat{\Psi}_{\text{nonlinear}}$ is the nonlinear thermoelastic part and $\hat{\psi}_{\text{str}}$ represents the energy stored due the evolving state variables of the plasticity model. The free energy corresponding to the nonlinear thermoelastic behavior is defined as

$$\tilde{\rho}\hat{\Psi}_{\text{nonlin}} = \frac{1}{2}\mathbb{C}_{ijkl}E_{eij}E_{ekl} - \mathbb{C}_{ijkl}E_{eij}\alpha_{kl} + \frac{1}{6}\mathbb{C}_{ijklmn}E_{eij}E_{ekl}E_{emn} - \frac{1}{2}\mathbb{C}_{ijklmn}E_{eij}E_{ekl}\alpha_{mn} + \hat{\psi}_T(T) \#(*)$$

Where $\boldsymbol{\alpha}$ is a second-rank tensor of stress-free thermal expansion, moreover, for the purposes of this investigation on pure aluminum, it is assumed that the thermal strains only contain a volumetric part (i.e., $\boldsymbol{\alpha} \approx \frac{1}{3}\alpha_v\mathbf{I}$), where α_v is the volumetric thermal expansion coefficient. Consequently, the $\mathbf{C}:\boldsymbol{\alpha}$ is directly analogous to the $\boldsymbol{\beta}\Delta T$ in Clayton [76] (i.e., $\boldsymbol{\beta} = \mathbf{C}:\mathbf{I}\alpha$, $\bar{\boldsymbol{\beta}} = \mathbf{C}:\mathbf{I}\alpha$). Moreover, the free energy stored within the microstructure during the evolution of the dislocation field is assumed to evolve at a fixed fraction of the rate of plastic work in accordance with a constant Taylor-Quinney parameter, χ , such that $\dot{\hat{\psi}}_{\text{str}} = (1 - \chi)(\tilde{\mathbf{S}}:\tilde{\mathbf{D}}_p)/\tilde{\rho}$. The value of unity is adopted in all the simulations in the current work. This approximation of the evolution of stored free energy combined with an expression for the conservation of energy leads to the common relationship for the evolution of temperature[29, 76, 77], i.e.,

$$\tilde{\rho}C\dot{T} = \tilde{\rho}D_{\text{mec}} - T\tilde{\boldsymbol{\beta}}_s:\tilde{\mathbf{D}}_e - J_e\Delta \cdot \mathbf{q} \#(\text{A.6})$$

where

$$\tilde{\boldsymbol{\beta}}_s = -\frac{\partial \tilde{\mathbf{S}}}{\partial T} \approx \boldsymbol{\beta} + \bar{\boldsymbol{\beta}}:\mathbf{E}_e \#(\text{A.7})$$

and

$$\tilde{\rho}D_{\text{mec}} = \tilde{\mathbf{S}}:\tilde{\mathbf{D}}_p - \tilde{\rho}\dot{\hat{\psi}}_{\text{str}} = \chi\tilde{\mathbf{S}}:\tilde{\mathbf{D}}_p \#(\text{A.8})$$

For the current simulations, involving ambient initial test temperatures (i.e., $T(t=0) = T_{ref}$) and small changes in temperature, we adopt a form the reference state of the free energy of $\hat{\psi}_T(T) =$

$-C_v T \ln\left(\frac{T}{T_{\text{ref}}}\right)$, which leads to a constant specific heat capacity at constant volume (i.e., $C = -T \frac{\partial^2 \psi}{\partial T^2} = -T \frac{\partial^2 \hat{\psi}_T}{\partial T^2} = C_v$).

Next, from Eqs. (A.2 - 4) and the additive decomposition of the Green-Lagrange strain in the reference configuration we decompose the nonlinear thermoelastic part into a term $\hat{\Psi}_{\text{vol}}$ that depends solely on the volumetric part of the deformation, and $\hat{\Psi}_{\text{cpl}}$, having contributions from both the volumetric and isochoric parts of the deformation. I.e.,

$$\hat{\Psi}_{\text{nonlin}} = \hat{\Psi}_{\text{vol}}(V, T) + \hat{\Psi}_{\text{cpl}}(\hat{\mathbf{E}}_e, V, T) \quad \#(A.9)$$

$$\tilde{\rho} \hat{\Psi}_{\text{vol}}(V, T) = \frac{1}{2} K \delta^2 - K \delta \alpha_v + \frac{1}{6} \bar{K} \delta^3 - \frac{1}{2} \bar{K} \delta^2 \alpha_v + \hat{\psi}_T(T) \quad \#(A.10)$$

And,

$$\begin{aligned} \tilde{\rho} \hat{\Psi}_{\text{cpl}}(\hat{\mathbf{E}}_e, V, T) = & \frac{1}{2} C_{ijkl} \hat{E}_{eij} \hat{E}_{ekl} + C_{ijkl} \bar{E}_{eij} \hat{E}_{ekl} - C_{ijkl} \bar{E}_{eij} \hat{\alpha}_{kl} - C_{ijkl} \hat{E}_{eij} \hat{\alpha}_{kl} - G_{ij} \hat{E}_{eij} \alpha_v + \\ & \frac{1}{6} C_{ijklmn} \hat{E}_{eij} \hat{E}_{ekl} \hat{E}_{emn} + \frac{1}{2} C_{ijklmn} \bar{E}_{eij} \bar{E}_{ekl} \hat{E}_{emn} + \frac{1}{2} C_{ijklmn} \hat{E}_{eij} \hat{E}_{ekl} \bar{E}_{emn} - \frac{1}{2} C_{ijklmn} \bar{E}_{eij} \bar{E}_{ekl} \hat{\alpha}_{mn} \\ & - \frac{1}{2} C_{ijklmn} \hat{E}_{eij} \hat{E}_{ekl} \alpha_{mn} - C_{ijklmn} \bar{E}_{eij} \hat{E}_{ekl} \alpha_{mn} \quad \#(A.11) \end{aligned}$$

Where, $K = \frac{1}{9} \mathbf{I} : \mathbf{C} : \mathbf{I}$, $\mathbf{G} = \frac{1}{3} \mathbf{C} : \mathbf{I}$, $\bar{K} = \frac{1}{27} (\mathbf{I} : \mathbf{C} : \mathbf{I}) : \mathbf{I}$ and $\bar{\mathbf{G}} = \frac{1}{9} \mathbf{I} : \mathbf{C} : \mathbf{I}$ are adopted for the sake of compact notation. For simplicity, the nonlinear coupled term can be written as

$$\begin{aligned} \tilde{\rho}\widehat{\Psi}_{\text{cpl}} = & \frac{1}{2}C_{ijkl}E_{ejj}E_{ekl} - C_{ijkl}E_{ejj}\alpha_{kl} + \frac{1}{6}C_{ijklmn}E_{ejj}E_{ekl}E_{emn} - \frac{1}{2}C_{ijklmn}E_{ejj}E_{ekl}\alpha_{mn} \\ & - \left[\frac{1}{2}K\delta^2 - K\delta\alpha_v + \frac{1}{6}\bar{K}\delta^3 - \frac{1}{2}\bar{K}\delta^2\alpha_v \right] \#(\text{A. 12}) \end{aligned}$$

This decomposition allows for the incorporation of a pressure, volume, temperature equation of state for capturing the volumetric part of the free energy, by replacing the volumetric part with the one from the EOS, (i.e., $\tilde{\rho}\widehat{\Psi}_{\text{vol}}(V, T) \leftarrow \tilde{\rho}\widehat{\Psi}_{\text{eos}}(V, T)$) such that the free energy is given by

$$\widehat{\Psi}(\mathbf{E}_e, T, \boldsymbol{\varrho}) = \widehat{\Psi}_{\text{eos}}(V, T) + \widehat{\Psi}_{\text{cpl}}(\widehat{\mathbf{E}}_e, V, T) + \widehat{\Psi}_{\text{str}}(\boldsymbol{\varrho}, T) \#(\text{A. 13})$$

The contribution to the stress in the intermediate configuration from the volumetric and coupled terms of the free energy are given from the state relations, leading to its additive decomposition (i.e., $\tilde{\mathbf{S}} = \mathbf{S}_{\text{eos}} + \mathbf{S}_{\text{cpl}}$), where the contribution from the EOS is given by

$$\mathbf{S}_{\text{eos}} = \tilde{\rho} \frac{\partial \widehat{\Psi}_{\text{eos}}}{\partial \mathbf{E}_e} = -J_e P_{\text{eos}} \mathbf{C}_e^{-1} \#(\text{A. 14})$$

and the contribution from the coupled volumetric and isochoric term is given by

$$\begin{aligned} \mathbf{S}_{\text{cpl}} = & \tilde{\rho} \frac{\partial \widehat{\Psi}_{\text{cpl}}}{\partial \mathbf{E}_e} = \mathbb{C} : (\mathbf{E}_e - \boldsymbol{\alpha}) + \frac{1}{2} \mathbf{E}_e : \mathbb{C} : \mathbf{E}_e - \mathbf{E}_e : \mathbb{C} : \boldsymbol{\alpha} \\ & - J_e^{\frac{2}{3}} \left[K(\delta - \alpha_v) + \bar{K} \left(\frac{1}{2} \delta^2 - \delta \alpha_v \right) \right] \mathbf{C}_e^{-1} \#(\text{A. 15}) \end{aligned}$$

The corresponding thermomechanical coupling tensor, $\tilde{\boldsymbol{\beta}}_s$, containing the contribution from the EOS is given by

$$\tilde{\boldsymbol{\beta}}_s = -\frac{\partial \tilde{\mathbf{S}}}{\partial T} \approx -J_e \frac{\partial P_{\text{eos}}}{\partial T} \mathbf{C}_e^{-1} + \boldsymbol{\beta} + \bar{\boldsymbol{\beta}} : \mathbf{E}_e - J_e^{\frac{2}{3}} (K\alpha_v + \bar{K}\delta\alpha_v) \mathbf{C}_e^{-1} \#(\text{A. 16})$$

Finally, the stress measure can be pulled back to the reference configuration via $\mathbf{S} = \mathbf{F}_p^{-1} \tilde{\mathbf{S}} \mathbf{F}_p^{-T}$ from which the first Piola Kirchhoff stress (used in our total-Lagrangian semi-discretization of the conservation of momentum[29]), is computed as $\mathbf{P} = \mathbf{F} \mathbf{S} = \mathbf{F}_e \tilde{\mathbf{S}} \mathbf{F}_e^{-T}$, and, the true Cauchy stress is $\boldsymbol{\sigma} = \mathbf{J}^{-1} \mathbf{P} \mathbf{F}^T = \mathbf{J}_e^{-1} \mathbf{F}_e \tilde{\mathbf{S}} \mathbf{F}_e^{-T}$.

Bryan Zuanetti: Conceptualization, Investigation, Methodology, Software, Visualization, Writing - Original Draft, Writing – Review & Editing. **Darby J. Luscher:** Resources, Conceptualization, Methodology, Software, Writing – Review & Editing **Kyle Ramos:** Resources, Conceptualization, Writing – Original Draft , Writing – Review & Editing. **Cynthia Bolme:** Resources, Conceptualization, Writing – Original Draft , Writing – Review & Editing.

Declaration of interests

The authors declare that they have no known competing financial interests or personal relationships that could have appeared to influence the work reported in this paper.

The authors declare the following financial interests/personal relationships which may be considered as potential competing interests

REFERENCES

1. Nguyen, T., S.J. Fensin, and D.J. Luscher, *Dynamic crystal plasticity modeling of single crystal tantalum and validation using Taylor cylinder impact tests*. International Journal of Plasticity, 2021: p. 102940.
2. Nguyen, T., D.J. Luscher, and J.W. Wilkerson, *A dislocation-based crystal plasticity framework for dynamic ductile failure of single crystals*. Journal of the Mechanics and Physics of Solids, 2017. **108**: p. 1-29.
3. Austin, R.A. and D.L. McDowell, *A dislocation-based constitutive model for viscoplastic deformation of fcc metals at very high strain rates*. International Journal of Plasticity, 2011. **27**(1): p. 1-24.

4. Liu, J., et al., *Mechanical behavior of ultrafine-grained/nanocrystalline titanium synthesized by mechanical milling plus consolidation: experiments, modeling and simulation*. International Journal of Plasticity, 2015. **64**: p. 151-163.
5. Nye, J.F., *Physical properties of crystals: their representation by tensors and matrices*. 1985: Oxford university press.
6. Ren, Z.-Y. and Q.-S. Zheng, *A quantitative study of minimum sizes of representative volume elements of cubic polycrystals—numerical experiments*. Journal of the Mechanics and Physics of Solids, 2002. **50**(4): p. 881-893.
7. Liu, C., *On the minimum size of representative volume element: an experimental investigation*. Experimental mechanics, 2005. **45**(3): p. 238-243.
8. Koohbor, B., S. Ravindran, and A. Kidane, *Experimental determination of Representative Volume Element (RVE) size in woven composites*. Optics and Lasers in Engineering, 2017. **90**: p. 59-71.
9. Ravindran, S., B. Koohbor, and A. Kidane, *Experimental characterization of meso-scale deformation mechanisms and the RVE size in plastically deformed carbon steel*. Strain, 2017. **53**(1): p. e12217.
10. Luscher, D., D.L. McDowell, and C. Bronkhorst, *Essential features of fine scale boundary conditions for second gradient multiscale homogenization of statistical volume elements*. International Journal for Multiscale Computational Engineering, 2012. **10**(5).
11. Walters, D.J., D.J. Luscher, and J.D. Yeager, *Considering computational speed vs. accuracy: Choosing appropriate mesoscale RVE boundary conditions*. Computer Methods in Applied Mechanics and Engineering, 2021. **374**: p. 113572.
12. Kanel, G., et al., *Effects of temperature on the flow stress of aluminum in shock waves and rarefaction waves*. Journal of Applied Physics, 2020. **127**(3): p. 035901.
13. Kanel, G., et al., *Effects of temperature and strain on the resistance to high-rate deformation of copper in shock waves*. Journal of Applied Physics, 2020. **128**(11): p. 115901.
14. Zaretsky, E. and G. Kanel, *Response of copper to shock-wave loading at temperatures up to the melting point*. Journal of Applied Physics, 2013. **114**(8): p. 083511.
15. Grunschel, S., R.J. Clifton, and T. Jiao. *Shearing resistance of aluminum at high strain rates and at temperatures approaching melt*. in *AIP Conference Proceedings*. 2012. AIP.
16. Kettenbeil, C., et al., *Pressure-Shear Plate Impact Experiments on Soda-Lime Glass at Pressures Beyond 20 GPa*, in *Dynamic Behavior of Materials, Volume 1*. 2019, Springer. p. 163-165.

17. Jiao, T., P. Malhotra, and R.J. Clifton. *IR temperature measurement in pressure-shear plate impact experiments*. in *AIP Conference Proceedings*. 2018. AIP Publishing LLC.
18. Strand, O., et al., *Compact system for high-speed velocimetry using heterodyne techniques*. *Review of Scientific Instruments*, 2006. **77**(8): p. 083108.
19. Barker, L.M. and R.E. Hollenbach, *Laser interferometer for measuring high velocities of any reflecting surface*. *Journal of Applied Physics*, 1972. **43**(11): p. 4669-4675.
20. Kim, K.S., R.J. Clifton, and P. Kumar, *A combined normal- and transverse-displacement interferometer with an application to impact of γ -cut quartz*. *Journal of Applied Physics*, 1977. **48**(10): p. 4132-4139.
21. Zuanetti, B., T. Wang, and V. Prakash, *A compact fiber optics-based heterodyne combined normal and transverse displacement interferometer*. *Review of Scientific Instruments*, 2017. **88**(3): p. 033108.
22. Kettenbeil, C., et al., *Heterodyne transverse velocimetry for pressure-shear plate impact experiments*. *Journal of Applied Physics*, 2018. **123**(12): p. 125902.
23. Zuanetti, B., et al., *Measurement of elastic precursor decay in pre-heated aluminum films under ultra-fast laser generated shocks*. *Journal of Applied Physics*, 2018. **123**(19): p. 195104.
24. Whitley, V., et al., *The elastic-plastic response of aluminum films to ultrafast laser-generated shocks*. *Journal of Applied Physics*, 2011. **109**(1): p. 013505.
25. Smith, R., et al., *High strain-rate plastic flow in Al and Fe*. *Journal of Applied Physics*, 2011. **110**(12): p. 123515.
26. Gurrutxaga-Lerma, B., et al., *The effect of temperature on the elastic precursor decay in shock loaded FCC aluminium and BCC iron*. *International Journal of Plasticity*, 2017. **96**: p. 135-155.
27. Klopp, R., R. Clifton, and T. Shawki, *Pressure-shear impact and the dynamic viscoplastic response of metals*. *Mechanics of Materials*, 1985. **4**(3-4): p. 375-385.
28. Frutschy, K. and R. Clifton, *High-temperature pressure-shear plate impact experiments on OFHC copper*. *Journal of the Mechanics and Physics of Solids*, 1998. **46**(10): p. 1723-1744.
29. Zuanetti, B., et al., *Dynamic Flow Stress of Pure Polycrystalline Aluminum: Pressure-Shear Plate Impact Experiments and Extension of Dislocation-based Modeling to Large Strains*. *Journal of the Mechanics and Physics of Solids*, 2020: p. 104185.
30. Kanel, G., *Spall fracture: methodological aspects, mechanisms and governing factors*. *International journal of fracture*, 2010. **163**(1): p. 173-191.

31. Garkushin, G., S. Razorenov, and G. Kanel, *Effect of structural factors on submicrosecond strength of D16T aluminum alloy*. Technical Physics, 2008. **53**(11): p. 1441-1446.
32. Vignjevic, R., et al., *Effects of orientation on the strength of the aluminum alloy 7010-T6 during shock loading: Experiment and simulation*. Journal of applied physics, 2002. **92**(8): p. 4342-4348.
33. Escobedo, J., et al., *Effects of grain size and boundary structure on the dynamic tensile response of copper*. Journal of Applied Physics, 2011. **110**(3): p. 033513.
34. Asay, J. and L. Barker, *Interferometric measurement of shock-induced internal particle velocity and spatial variations of particle velocity*. Journal of Applied Physics, 1974. **45**(6): p. 2540-2546.
35. Mescheryakov, Y.I., A. Divakov, and N. Zhigacheva, *Shock-induced structural transitions and dynamic strength of solids*. International journal of solids and structures, 2004. **41**(9-10): p. 2349-2362.
36. Divakov, A.K., T.A. Khantuleva, and Y.I. Mescheryakov, *Kinetics of Mesostructure and Reloading Behavior of Dynamically Compressed Solids*. AIP Conference Proceedings, 2004. **706**(1): p. 553-556.
37. Bolme, C. and K. Ramos, *Line-imaging velocimetry for observing spatially heterogeneous mechanical and chemical responses in plastic bonded explosives during impact*. Review of Scientific Instruments, 2013. **84**(8): p. 083903.
38. Smith, R., et al., *Heterogeneous flow and brittle failure in shock-compressed silicon*. Journal of Applied Physics, 2013. **114**(13): p. 133504.
39. Meyers, M. and M. Carvalho, *Shock-front irregularities in polycrystalline metals*. Materials Science and Engineering, 1976. **24**(1): p. 131-135.
40. Lipkin, J. and J. Asay, *Reshock and release of shock-compressed 6061-T6 aluminum*. Journal of applied physics, 1977. **48**(1): p. 182-189.
41. Huang, H. and J. Asay, *Compressive strength measurements in aluminum for shock compression over the stress range of 4–22 GPa*. Journal of Applied Physics, 2005. **98**(3): p. 033524.
42. Barber, J. and K. Kadau, *Shock-front broadening in polycrystalline materials*. Physical Review B, 2008. **77**(14): p. 144106.
43. Krasnikov, V. and A. Mayer, *Modeling of plastic localization in aluminum and Al–Cu alloys under shock loading*. Materials Science and Engineering: A, 2014. **619**: p. 354-363.

44. Huang, S. and R.J. Clifton, *Dynamic plastic response of OFHC copper at high shear strain rates*, in *Macro-and Micro-Mechanics of High Velocity Deformation and Fracture*. 1987, Springer. p. 63-74.
45. Casem, D.T., et al., *High-rate mechanical response of aluminum using miniature Kolsky bar techniques*, in *Dynamic Behavior of Materials, Volume 1*. 2018, Springer. p. 147-153.
46. Austin, R.A. and D.L. McDowell, *Parameterization of a rate-dependent model of shock-induced plasticity for copper, nickel, and aluminum*. *International journal of plasticity*, 2012. **32**: p. 134-154.
47. Lloyd, J., et al., *Simulation of shock wave propagation in single crystal and polycrystalline aluminum*. *International Journal of Plasticity*, 2014. **60**: p. 118-144.
48. Luscher, D.J., et al., *A dislocation density-based continuum model of the anisotropic shock response of single crystal α -cyclotrimethylene trinitramine*. *Journal of the Mechanics and Physics of Solids*, 2017. **98**: p. 63-86.
49. Luscher, D.J., et al., *Coupling continuum dislocation transport with crystal plasticity for application to shock loading conditions*. *International Journal of Plasticity*, 2016. **76**: p. 111-129.
50. Gilman, J.J., *Micromechanics of flow in solids*. 1969, New York: New York, McGraw-Hill.
51. Blaschke, D.N., *Averaging of elastic constants for polycrystals*. *Journal of Applied Physics*, 2017. **122**(14): p. 145110.
52. Thomas, J.F., *Third-Order Elastic Constants of Aluminum*. *Physical Review*, 1968. **175**(3): p. 955-962.
53. Raju, S., K. Sivasubramanian, and E. Mohandas, *The high temperature bulk modulus of aluminium: an assessment using experimental enthalpy and thermal expansion data*. *Solid state communications*, 2002. **122**(12): p. 671-676.
54. Fredenburg, D.A., T.D. Aslam, and L.S. Bennett, *(U) A Gruneisen Equation of State for TPX. Application in FLAG*. 2015, Los Alamos National Lab.(LANL), Los Alamos, NM (United States).
55. Marsh, S.P. and L. Los Alamos Scientific, *LASL shock Hugoniot data*. 1980, Berkeley: Berkeley : University of California Press.
56. Austin, R.A., *Elastic precursor wave decay in shock-compressed aluminum over a wide range of temperature*. *Journal of Applied Physics*, 2018. **123**(3): p. 035103.
57. Blaschke, D.N. and D.J. Luscher, *Dislocation drag and its influence on elastic precursor decay*. arXiv preprint arXiv:2101.10497, 2021.

58. Zuanetti, B., T. Wang, and V. Prakash, *Dynamic behavior of polycrystalline metals under combined pressure and shear loading at elevated temperatures*. AIP Conference Proceedings, 2020. **2272**(1): p. 100024.
59. Ma, A. and F. Roters, *A constitutive model for fcc single crystals based on dislocation densities and its application to uniaxial compression of aluminium single crystals*. Acta materialia, 2004. **52**(12): p. 3603-3612.
60. Hart, K.A. and J.J. Rimoli, *Generation of statistically representative microstructures with direct grain geometry control*. Computer Methods in Applied Mechanics and Engineering, 2020. **370**: p. 113242.
61. Hart, K.A. and J.J. Rimoli, *MicroStructPy: A statistical microstructure mesh generator in Python*. SoftwareX, 2020. **12**: p. 100595.
62. Arvo, J., *Fast random rotation matrices*, in *Graphics gems III (IBM version)*. 1992, Elsevier. p. 117-120.
63. Zavattieri, P., P. Raghuram, and H. Espinosa, *A computational model of ceramic microstructures subjected to multi-axial dynamic loading*. Journal of the Mechanics and Physics of Solids, 2001. **49**(1): p. 27-68.
64. Mohan, N., et al., *Modeling Microstructural Effects on Heterogeneous Temperature Fields within Polycrystalline Explosives*. Propellants, Explosives, Pyrotechnics, 2021.
65. Luscher, D.J., et al. *Implementation of a dislocation-density based single-crystal model into a continuum shock hydrodynamics code*. in *AIP Conference Proceedings*. 2018. AIP Publishing LLC.
66. Pyle, D.M., et al., *Effect of 3D grain structure representation in polycrystal simulations*. Computational Mechanics, 2013. **52**(1): p. 135-150.
67. Bishop, J.E., et al., *Direct numerical simulations in solid mechanics for understanding the macroscale effects of microscale material variability*. Computer methods in applied mechanics and engineering, 2015. **287**: p. 262-289.
68. Belytschko, T., et al., *Nonlinear Finite Elements for Continua and Structures*. 2014, New York: New York: John Wiley & Sons, Incorporated.
69. Felippa, C.A., K.-C. Park, and C. Farhat, *Partitioned analysis of coupled mechanical systems*. Computer methods in applied mechanics and engineering, 2001. **190**(24-25): p. 3247-3270.
70. Zuanetti, B., T. Wang, and V. Prakash, *Plate Impact Investigation of the Dynamic Response of Commercial Tungsten Carbide Under Shock-induced Compression and Combined Compression-and-Shear loading*. International Journal of Impact Engineering, 2019.

71. Zuanetti, B., T. Wang, and V. Prakash, *Mechanical response of 99.999% purity aluminum under dynamic uniaxial strain and near melting temperatures*. International Journal of Impact Engineering, 2018. **113**: p. 180-190.
72. Nguyen, T., D.J. Luscher, and J.W. Wilkerson, *The role of elastic and plastic anisotropy in intergranular spall failure*. Acta Materialia, 2019. **168**: p. 1-12.
73. Zaretsky, E. and G.I. Kanel, *Effect of temperature, strain, and strain rate on the flow stress of aluminum under shock-wave compression*. Journal of Applied Physics, 2012. **112**(7): p. 073504.
74. Yuan, F., N.-S. Liou, and V. Prakash, *High-speed frictional slip at metal-on-metal interfaces*. International Journal of Plasticity, 2009. **25**(4): p. 612-634.
75. Luscher, D.J., et al., *A model for finite-deformation nonlinear thermomechanical response of single crystal copper under shock conditions*. Journal of the Mechanics and Physics of Solids, 2013. **61**(9): p. 1877-1894.
76. Clayton, J.D., *Nonlinear Eulerian thermoelasticity for anisotropic crystals*. Journal of the Mechanics and Physics of Solids, 2013. **61**(10): p. 1983-2014.
77. Luscher, D.J., et al., *On computing the evolution of temperature for materials under dynamic loading*. International Journal of Plasticity, 2018. **111**: p. 188-210.